UNIVERSITY OF CALIFORNIA, SAN DIEGO

Heat Flux Manipulation using Thermal Meta-materials

A dissertation submitted in partial satisfaction of the
requirements for the degree
Doctor of Philosophy

in

Engineering Sciences (Mechanical Engineering)

by

Rahul S. Kapadia

Committee in charge:

Professor Prabhakar Bandaru, Chair
Professor Renkun Chen
Professor Massimiliano Di Ventra
Professor Jan Kleissl
Professor Kalyanasundaram Seshadri

2014

The dissertation of Rahul S. Kapadia is approved, and it is acceptable in quality and form for publication on microfilm and electronically:

_____

_____

_____

_____

_____

Chair

University of California, San Diego

2014

DEDICATION

To my Parents, who provided me the best opportunities a child could ever have asked for, my Sister for being always there for me and lastly to Atreyi for being my soul mate

EPIGRAPH

The woods are lovely, dark and deep,
But I have promises to keep,
And miles to go before I sleep,
And miles to go before I sleep.
—Robert Frost

TABLE OF CONTENTS

LIST OF FIGURES

LIST OF TABLES

ACKNOWLEDGEMENTS

I want to take this opportunity to thank the countless people who have supported my through my journey through graduate school. First and foremost, I am greatly thankful to my advisor, Dr. Prabhakar Bandaru for accepting me in his research group, and for guiding me through the last four years. During this time, I have learnt countless things from him, foremost among them a development of a scientific intuition. I was also very lucky to have his trust and confidence for making lot of my experimental decisions by myself, and having him to fall back on whenever something went wrong. Without his guidance and words of encouragement, I am sure I would not have been able to complete my PhD. I am also grateful to my dissertation committee, which includes my advisor, Prof. Renkun Chen, Prof. Jan Kleissl, Prof. Kalyanasundaram Seshadri and Prof. Massimiliano Di Ventra, for their contributions which held my work to the highest standards of scientific rigor, in the spirit of academic tradition. I have deep gratitude for Prof. Renkun Chen for providing guidance for setting up the steady state heat conductivity measurement setup, and for Prof. Jan Kleissl for allowing me to borrow the IR Camera which helped me tremendously at the beginning of my heat flux measurement experiments.

I could not have completed my graduate school without the Teaching Assistant opportunities I got at the Mechanical & Aerospace Engineering Department. I am greatly thankful to Prof. Kalyanasundaram Seshadri, Prof. Renkun Chen, Prof. Yousef Bahadori, Prof. Farhat Beg, Prof. Ratnesh Lal, Prof. Robert Cattolica & Prof. Carlos Coimbra for appointment me as a TA in their respective classes. I am greatly indebted to Nicholas Busan, for giving me the opportunity to be a TA for MAE 170, and what started as a professional relationship has turned into a lifelong friendship. In the same vein, I am also thankful to Michael Watson. Having been a head TA for MAE 170 for 10 quarters has taught me lot of very important lessons in life including a deeper appreciation for teaching and the nuances attached to it.

I am also very appreciative of lot of my colleagues, who became friends as we all progressed along in graduate school. Foremost among them to Max Aubain,

from being a Head TA for MAE 170 in my first quarter of being a TA, to guiding me in my earlier years in the research group and always being a really insightful sounding board for refining my ideas. I am also very thankful to Brian Louie for working with me initially in setting up the steady state experimental setup, without his lab view skills and original work, the project would have take much longer than it did. I am also appreciative of insightful conversations and friendly banter with my lab mates - Max, Paothep, Anna, Rajaram, Hasan, Krishna, Byung and David. I would also like to acknowledge assistance I received from the undergraduate interns who worked for us in the lab: Thaer Karjah, Hochul Kim and Timothy Lee.

Lot of my experimental work would not have been possible without the guidance, help and assistance I got from the MAE Machine Shop staff. Tom Chalfant for his sheer ingenuity and unwavering support to device countless experimental setups, without which none of my experiments would have been possible. I am also thankful to Isaiah Freeksen for his extensive help in machining lot of my components. I am also thankful to Matthew McNelis from SOLEC-Solar Energy Corp for providing their low emissivity paint LO/MIT-II MAX for our experiments.

I was very lucky to have served as the President of the Graduate Student Association at UC San Diego. This opportunity fulfilled one of my biggest dreams and has shaped me the way I am today. I was always amazed by the support I received from the administration, and their utmost desire to make this university a better place for students. For this, I am greatly thankful to Dean of Graduate Students Dr. Kim Barrett, Chancellor Dr. Pradeep Khosla & Interim Vice Chancellor of Student Affairs Dr. Alan Houston. I am also thankful to the past and present executive council of GSA for the support, and to the greater GSA Council for putting their faith in me while electing me to be their Vice President Financial Affairs and subsequently their President.

Finally, I want to take this opportunity to thank my parents. I am sure no words of mine can be commensurate for the support I have got from them in the last 29 years, but I hope fulfilling one of the biggest dreams of theirs and mine, by getting a PhD will be a small consolation. I am also thankful to my sister, for

being a beacon of support all my life, and to her and my brother-in-law for being my local parents in this country. Lastly, I am deeply appreciative of the love and support I found in graduate school from Atreyi. From encouraging me to continue at UC San Diego for my PhD, to being there next to me all along the journey, the only way I will be able to repay you is by marrying you.

Most of the work described in chapter 2 & 3 has been adopted from Kapadia, R. S., Louie, B. M., Bandaru, P. R., "The influence of carbon nanotube aspect ratio on thermal conductivity enhancement in nanotube-polymer composites", *Journal of Heat Transfer*, v.136, 011303, 2013.

Some materials from chapter 4, 5, 6, 7, & 8 are currently being prepared for submission for publication. The dissertation author, Rahul S. Kapadia was the primary investigator and author of this material.

VITA

2006	B. E. Mechanical Engineering Nirma Institute of Technology, Gujarat University, Ahmedabad, India
2010	M. S. Engineering Sciences (Mechanical Engineering) University of California, San Diego
2014	Ph. D. Engineering Sciences (Mechanical Engineering) University of California, San Diego

PUBLICATIONS

Kapadia, R. S., Louie, B. M., Bandaru, P. R., "The influence of carbon nanotube aspect ratio on thermal conductivity enhancement in nanotube-polymer composites", *Journal of Heat Transfer*, v.136, 011303, 2013.

Kim, B. -W, Park, S.-H., Kapadia R. S., Bandaru, P. R., "Evidence of percolation related power law behavior in the thermal conductivity of nanotube/polymer composites", *Applied Physics Letters*, v.102, 243105, 2013.

ABSTRACT OF THE DISSERTATION

Heat Flux Manipulation using Thermal Meta-materials

by

Rahul S. Kapadia

Doctor of Philosophy in Engineering Sciences (Mechanical Engineering)

University of California, San Diego, 2014

Professor Prabhakar Bandaru, Chair

The control and manipulation of heat flux could lead to reduced energy losses as well as pave the way for creation of thermal analogues to electronic and optical elements such as diodes and lenses. Additionally, the developed principles can be employed for enhancing thermal to electrical energy conversion efficiencies as well as for efficient cooling.

While recent work on thermal energy control seeks to understand atomic scale paradigms that control transport processes, e.g., phononics, with the broad objective of manipulating heat flow with electronic analogs and beyond, our approach is nominally distinct and involves ideas borrowed from transformation optics. The principle that heat flux takes the path of least thermal resistance, analogous to the Fermat principle for light, was used to fabricate thermal devices,

which could be used to concentrate heat similar to a converging lens. Finite Element analysis (FEA) based simulations as well as analytical relations were used to trace the path of heat flow in the thermal lens.

For demonstrating such effects experimentally, fabricated thermal lenses consisted of a multi-layered structure made of carbon nanotube (CNT) polymer composites, constituted from layers with gradually increasing CNT composition and concomitant increased thermal conductivity. The heat flux concentration, due to a temperature gradient across the thermal lens was monitored through a infrared (IR) imaging technique, and found to be in excellent accord with the simulations. From our experiments, we show 40 % increase in flux concentration using a rectangular geometry and a 50 % increase using a reducing geometry setup, which was transduced to electrical energy, through a thermoelectric generator.

We have also designed a thermal homogenizer using thermal meta-materials design strategies to ensure uniform heat flux concentration at a particular area / cross-section, which was demonstrated experimentally.

Our results pave the way for further understanding of ways to control and manipulate heat propagation

1 Introduction

In thermodynamics, heat is defined as energy transfer due to temperature gradients. Heat transfer takes place through three fundamental modes - Conduction, Convection and Radiation. Conduction occurs through varied phenomenon as molecular collision in gases, lattice vibrations in crystals and flow of electrons in metals. Convection is transport of energy by bulk motion of a medium. Radiation occurs in terms of proportion of electromagnetic waves or in terms of phonons. [1]

In solids, the heat conduction is generally considered to be through phonons. A phonon is a quasiparticle representing the quantization of the modes of lattice vibrations of periodic, elastic crystal structures of solids. The concept of Phonon was first introduced by Russian physicist Igor Tamm. A collective behavior of phonons can be analyzed through definitions of their wave vector determined energy levels. Such dispersion relations are also used to describe other physical phenomenon mainly optical and electrical transport.

Optical and electrical transport have been extensively studied and a very strong understanding has been developed resulting in many breakthroughs. These understandings have resulted in design of various devices. For optics, there are lot of devices starting from basic lens and mirrors going all the way to more complicated structures such as optical wave guides. For electricity, there are devices such as PN junctions, rectifiers, diodes among others. Compared to these two fields, the field of heat conduction has remained very bare. One such device was proposed by Chauncey Starr in 1935 in form of a thermal rectifier. [2]

One main reason of lack of thermal conduction devices is that it indeed is substantially more difficult to control a priori the flow of heat in a solid than it is to control the flow of electrons. The source of this imbalance is that, unlike electrons,

the carriers of heat the phonons are quasi-particles in the form of energy bundles that possess neither a bare mass nor a bare charge. [3]

Much recent work on thermal energy control seeks to understand atomic scale paradigms that control transport processes, e.g., phononics, with the broad objective of manipulating heat flow with electronic analogs and beyond.[3] Due to the overtly complicated nature of phonons, and their still relatively immature understanding, I have tried to focus more on using macroscopic relations to study and understand heat conduction control. Tan and Holland have discussed extensively how heat like electricity and light follow the path of least thermal resistance. [4]

Referring to the figure 1.1, a variational principle can be formulated for heat conduction in a continuous medium. For two fixed points P & Q in a the x-y plane, if heat flows from P to Q, the path of heat conduction would be that along which the thermal resistance is minimum / extremum. The thermal resistance per unit length (dl) can be defined as $Rl_{th} = 1 \,/\, \kappa A$, where A is the cross-sectional area of the flux tube between P & Q, and κ is the thermal conductivity of the medium. The total thermal resistance along the path can then be given by integral $\int dl/\kappa A$.

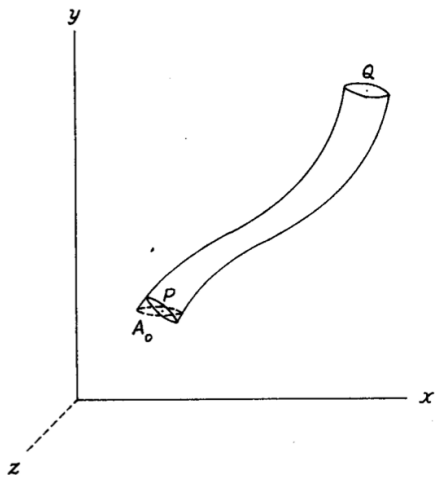

Figure 1.1: Propagation of heat flow in a medium with thermal conductivity κ [4].

The exact minimization would be based on the arrangement of media/materials

through which heat flux propagation occurs. It is the proposed that the constitutive material character (κ) as well as the extensive parameters such as the thermal traversal length (L) as well as the area (A) can be suitably adjusted to achieve the desired thermal flux propagation direction. Consequently, thermal energy orientation could be accomplished leading to novel functionalities such as energy focusing or dispersion akin to paradigms familiar from basic optical lenses.

Simplifying the earlier relation, we know that the fundamental law governing heat conduction at macro scale was proposed by French mathematical physicist Jean Baptiste Joseph Fourier in 1822. For a steady state (time invariant) conditions, this is given by

$$q = -\kappa \nabla T \tag{1.1}$$

Here q is the heat flux with units of W/m^2, while κ is the thermal conductivity of the material, and T is the temperature. Another form of the equation in terms of Heat - Q in one dimension is given by

$$Q = -\kappa A \frac{dT}{dx} \tag{1.2}$$

where A is the cross-section area of the conductor. The negative sign is due to the consideration that heat conduction occurs in the direction of decreasing temperature.

Georg Ohm modeled conduction of electricity similar to Fourier law and derived the following relation between electrical current (I), potential difference (V) and electrical resistance (R_e) as

$$I = \frac{V}{R_e} \tag{1.3}$$

Comparing these two equations, we see a similarity in the form. We can define thermal resistance as $(R_{th}) = dx \ / \ (\kappa A)$.

Thus just as electricity follows the path of least electrical resistance (R_e), conductive heat flux follows the path of least thermal resistance (R_{th}).

2 Experimental Setup for Thermal Conductivity Measurement

Thermal conductivity measurements are generally performed using two methods - Steady state measurements and Transient measurements. Steady state measurements as the name suggest are measurements, which are performed once a steady state is reached for the heat conduction, while in transient measurement methods, measurements are taken as a function of time. Steady state measurements are generally more accurate, but take a long time to perform due to the need for the heat conduction phenomenon to reach a steady state. These time delays sometimes can take upwards of few hours especially in cases of low thermal conductivity / low specific heat samples like polymers. Transient measurements in comparison are much faster and can be performed in matter of few minutes.

Some examples of steady state measurement methods are Guarded Hot-plate method and Longitudinal Bar method[5].

Examples of transient methods are Laser Flash diffusivity, 3 ω[6] among others. These methods are generally more expensive and complicated to setup. Also lot of these methods need specific conditions of samples being measured, e.g. Laser Flash diffusivity method is dependent on optical and emission properties of the materials and thus its difficult to use for materials with unknown properties. These methods also need a greater complicity in preparation of samples for the measurements, e.g. 3 ω methods requires the need to deposit metal lines on the sample surface to act as heater and thermometer.

For our measurements, we decided to model a setup similar to a guarded hot plate method based on ASTM E 1225 & D 5470 standards [7, 8]. The original rationale behind using this method was the availability of equipment in the lab, and inherent confidence we had in using a steady state method. Also we decided to put the complete experimental setup inside a Vacuum chamber to avoid the need for having a guarded plate. We use a custom 32 connector feed through for the chamber for Thermocouple and power connections.

For our setup, we use two stainless steel reference bars of 4 cm length and having a cross-sectional dimension of 1.4 cm x 1.4 cm. The specific length and materials of the bars was chosen with respect to the materials being tested so as to keep equivalent thermal resistance (l/κ) of the reference bars to the samples being tested to ensure similar values of temperature drop across the reference bars as well as the sample. For performing the measurement, we need to get the heat flux (q) passing through the reference bars. Measuring the temperature drop (ΔT) across the sample length, we can then use Fourier law to calculate the thermal conductivity of the sample as shown below.

$$\kappa_{sample} = q\frac{t}{\Delta T_{sample}} \tag{2.1}$$

To measure the heat flux in the reference bars, we use 3 K-type thermocouples in each of them and use published values of thermal conductivity for stainless steel.

$$q = \kappa_{SS}\frac{\Delta T_{top/bottom}}{l} \tag{2.2}$$

Here l is the distance between 1st and 3rd thermocouples.

K-type thermocouples were chosen as they have the highest accuracy in temperature range we were going to consider. Heat flux from the top and the bottom bars was measured, and the average was taken for our subsequent calculations. To measure the temperature drop across the samples, we use two more thermocouples connected very close ($\sim$ 1 mm) to reference bar sample interface in the reference bar. Using the previously measured Temperature gradient, we

extrapolate the exact temperature at the top and bottom surface of the sample.

$$T_{surface} = T_{measured} \pm d\frac{\Delta T_{top/bottom}}{l} \tag{2.3}$$

Here d is the distance of the thermocouple from the respective edge.

Thus with all these quantities we can calculate the thermal conductivity of the sample using a 1-dimensional Fourier law equation denoted earlier.

This setup due to high length to the cross-section dimensions ensures setup of a 1 Dimension heat flow in the setup, and thus ensures the applicability of 1 Dimensional Fourier Law equation.

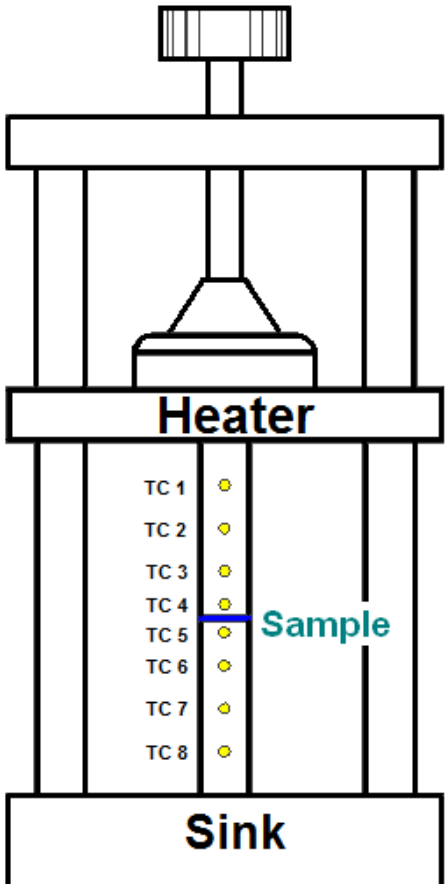

Figure 2.1: Schematic of experimental setup for the thermal conductivity (κ) measurement of the nanotube-polymer composite. The heat flux, (q) was deduced from the thermocouple recordings in the top and bottom stainless steel bars.

We use 40 gauge TC wires to minimize the conductive heat loss from the

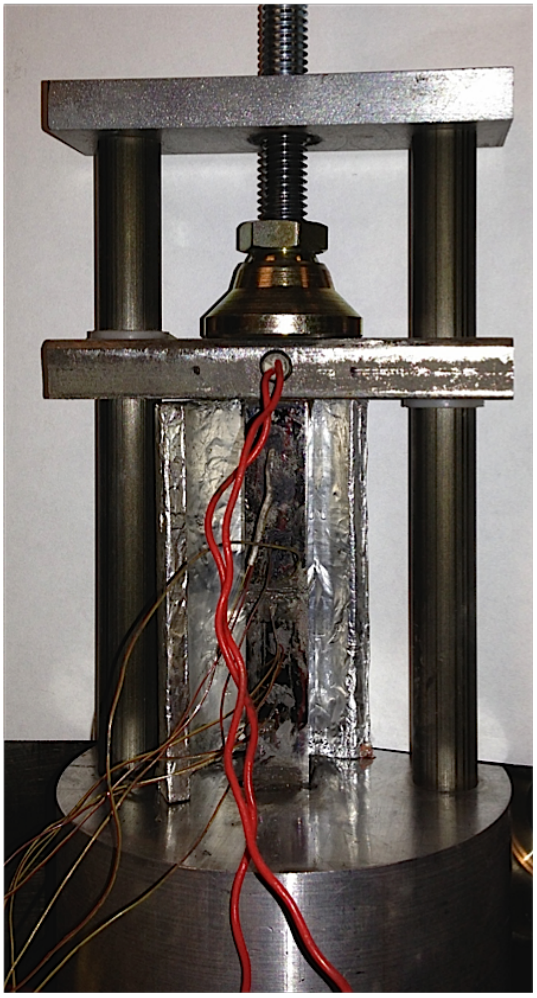

Figure 2.2: Picture of actual setup seen with 8 Thermocouples

wires. To attach the TC wires to the reference bars, we drilled holes up to the center of the cross-section, and then used Graphite pencil leads along with Thermal paste to ensure good contact and accurate temperature measurements. A cartridge heater was used in the top block as the heater. The bottom reference bar was attached to an Aluminum stock, which was used as a sink. The reference bars side surfaces were micro-polished to minimize radiative losses to a surface finish of $\sim$ 3 Micron. The bars were also surrounded by external Aluminum radiation shield to minimize radiative losses. We also machined notches in the top heater block as well as the bottom sink to ensure proper vertical positioning of the complete setup.

The sample thickness (t) in this setup is quite important. Using a Vernier caliper we observed a 5 - 10% discrepancy in measurement of the sample thickness, which was to the tune of 1.5 2 mm. As calculated thermal conductivity value is directly dependent on the measured thickness, we had to explore options to reduce this error in our measurement. After further deliberations, we used an in-house designed and fabricated dial gauge setup with accuracy of 25 Microns to measure the thickness of the sample schematically seen in figure 2.3. Using this setup we noticed a less than 1% variation in the measured thickness both of rigid as well as softer samples.

Interface resistance between the sample and the reference blocks play a very important part in our measurements. It has been shown [9] that interface resistance depends on surface finish of surfaces in contact and also the contact pressure. The complete setup was torqued to a set value to ensure minimum thermal contact resistance. We tested the complete setup with different torque values starting from 5 inch-lb going all the way to 25 inch-lb, and decided on a value of 15 inch-lb, which ensured minimum interface thermal resistance. To further reduce contact resistance, we used Arctic Silver 5, a commercially used thermal interface material in between all our contact surfaces. Finally all the contact surfaces were polished to 1 Micron surface finish by a micro-polishing system.

All tests were performed in a Vacuum chamber at pressure of $\sim$ 10 mTorr to ensure minimum convective losses. We estimated convective losses from the

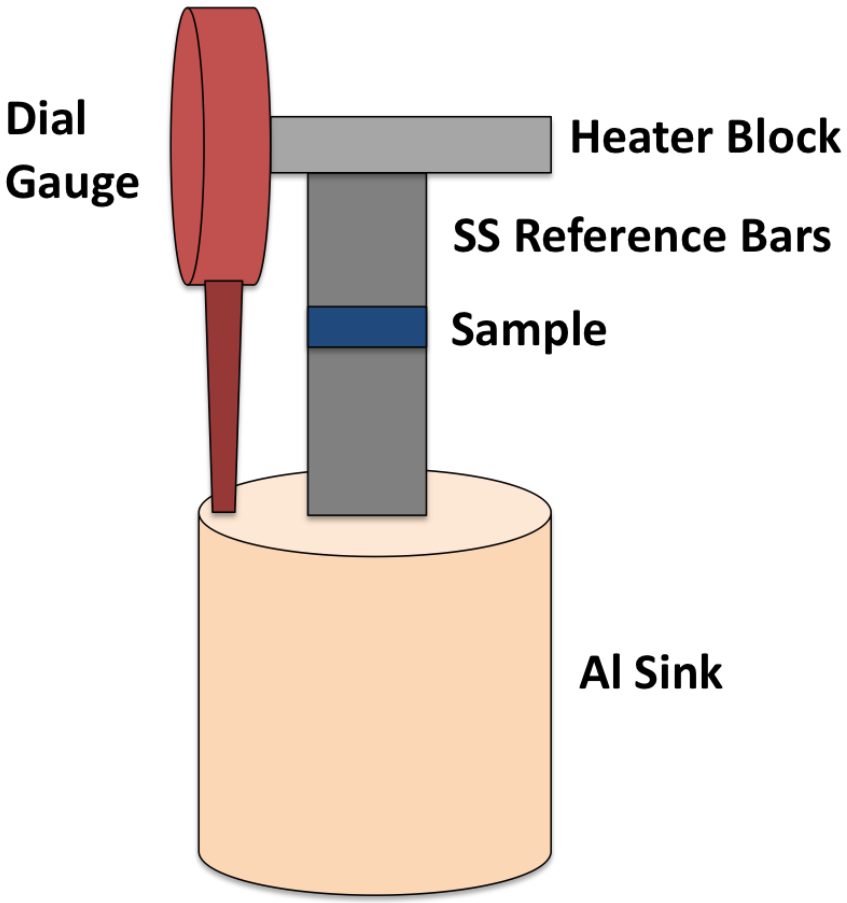

Figure 2.3: Dial gauge setup used to measure sample thickness

setup by getting values of the convective heat transfer co-efficient at 10 mTorr to be less than 5% of the conductive heat flus. We also estimate the radiative heat flux losses to be at most 5% of the total conductive heat flux by using values of emissivity of polished stainless steel and taking into account the effects of the radiation shield. Effects of radiation shield were also observed in the experiments. Before implementation of radiation shield, polishing of surfaces, and thicker 22 Gauge Thermocouple wires, the difference between heat flux in the top and bottom block was observed to be almost 40% and resulting thermal conductivity value variation for calibration was almost 30%. After the above-mentioned modifications, the final observed difference was around 5% proving less than 10% convective and radiative losses.

We also performed Finite Element Analysis using Comsol Multiphysics for our setup and observe the effects of convective and radiative losses on the measured thermal conductivity. Using the temperature values from the simulation, we re-calculate the thermal conductivity of the sample, and notice a less than 5% variation in the thermal conductivity values.

Steady state conditions were ensured through requiring the temperature measurement fluctuations to be less than 0.1 K over 10 minutes as defined in the ASTM standards [7, 8]. For low thermal conductivity samples, it generally took at least 15 hours to reach a desired steady state condition. Thus we generally ran simulations for longer periods $\sim$ 24 hours, and then took data for over 10 minutes to average out random errors.

All temperature measurements were recorded using a Keithley 2700 Digital Multimeter Data Acquisition and Data logging System with Keithley 7700, a 20-Channel, Differential Multiplexer Module with inbuilt cold junction compensation. A custom made NI LabVIEW VI was used to measure and record the 8 temperatures and also show instantaneous display of the thermal conductivity of the sample shown in figure 2.4. Subsequently the temperature data generated by the LabView was analyzed by Matlab to calculate the thermal conductivity of the sample along with its uncertainty being calculated primarily from the uncertainty associated with the k-type thermocouples.

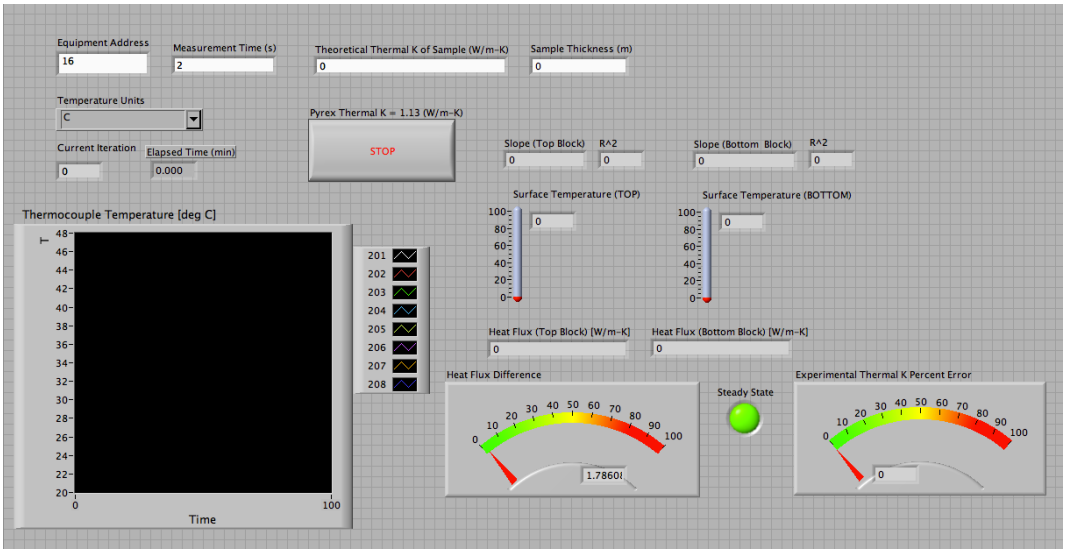

Figure 2.4: Screenshot of LabVIEW VI used to capture temperature measurements.

We have taken into account both systematic and random errors in our experiment. Systematic errors arise from the TC measurements for temperatures. We take into account a 0.75% uncertainty from the specifications of our TC (from Omega, Inc.) in our temperature measurement. Using this uncertainty ($u(T)$), we then calculate the uncertainty in the heat flux ($u(q)$) in the reference bars and the extrapolated temperatures of the top and the bottom surfaces of the sample. Subsequently using these calculations, we can calculate the uncertainty in thermal conductivity ($u(\kappa)$) by the following:

$$u(\kappa) = \left(\frac{q_{avg}t}{T_{top}}u(T_{top})\right)^2 + \left(\frac{q_{avg}t}{T_{bottom}}u(T_{bottom})\right)^2 + \left(\frac{t}{T_{top} - T_{bottom}}u(T_{q_{avg}})\right)^2$$

The estimate of random errors was done through standard deviation values of measurements of three sets of samples for each specific sample type.

The experimental setup was calibrated with Pyrex 7740 and Teflon PTFE samples, where κ was determined to be 1.14 ± 0.08 W/mK and 0.23 ± 0.01 W/mK, respectively and compares to within $\pm$ 5% of published values[10, 11]

Most of the work described in this chapter has been adopted from Kapadia, R. S., Louie, B. M., Bandaru, P. R., "The influence of carbon nanotube aspect ratio on thermal conductivity enhancement in nanotube-polymer composites", *Journal of Heat Transfer*, v.136, 011303, 2013.

3 Polymer Composite Thermal Conductivity Measurements

We wish to characterize thermal conductivity of polymer composites previously synthesized in our laboratory. The rational behind using Carbon Nanotubes as fillers in a base Polymer matrix, is it to use the inherently high aspect ratio which provide enhanced surface area resulting in high thermal and electrical conductivities as well as greater mechanical strength of the composites. Thus these properties can then be controlled by changing the CNT content in the composite.

3.1 Sample Preparation

We use a RET (reactive ethylene terpolymer - Elvaloy 4170) polymer from DuPont for our experiments. This copolymer consists of three distinct monomers, ethylene backbone which provides corrosion resistance, n-butyl acrylate, which provides elastomeric characteristics, and glycidyl methacrylate (GMA) which adds epoxide functionality, which can be seen in figure 3.1.

The traditional method of producing a thermally conductive polymer is to mix high concentrations of metal fillers (aluminum or copper), -around 50 volume percent, resulting in an order of magnitude increase in their thermal conductivity. For our samples, we use Multiwalled Carbon Nanotubes (MWNT) which have been functionalized with a -COOH functional group as the filler particles. We have chosen this specific combination of Polymer and the functionalized MWCNT, as the presence of the epoxide constituent on the polymer bonds with the -COOH group on the MWCNT forming robust ester-bonds, as was confirmed through

Fourier Transform Infrared (FTIR) spectroscopy [12, 13]. We believe this plays a crucial part in the polymers ability to be thermally conductive because it provides an anchor for the CNTs to bond to the polymer chain. This also helps in ensuring the filler particles get uniformly distributed in the polymer matrix.

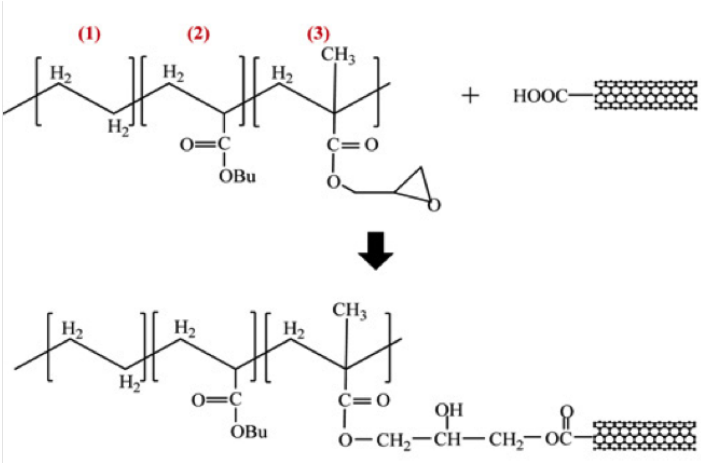

Figure 3.1: Figure showing structure of RET and also how the -COOH functionalized MWCNT can be bonded to the epoxide functional group

Fabrication of RET - CNT polymer samples has been discussed quite extensively in prior work [12, 13, 14].

To prepare the polymer, RET granules were blended in Toluene and heated for 2 hours at 60 °C with continuous stirring. Concurrently MWCNTs were dispersed and blended in Toluene and sonicated using a Sonics VCX 750 for 10 minutes. These 2 mixtures were subsequently combined and ultrasonicated again for 1 hour. This sonication step ensures uniform dispersing of the filler particles in the RET base and also ensures bonding between the -COOH functional groups with the epoxide bonds in the polymer. Subsequently the complete mixture is continuous stirred for 2 more hours to remove excess Toluene. Finally the mixtures is transferred to a glass dish and moved to a Vacuum oven to degas Toluene at ∼1 mTorr pressure and 40 °C for about 12 hours. We ensured the curing of the polymer through our processing treatments as per the manufacturers recommendations. Finally we end up with a thin film of the composite which can be subsequently made into samples of desired thickness using a Hot Press from Carver

Inc.

A uniform dispersion of the MWCNTs was recorded across the cross section of our composite (through considering SEM micrographs of sample sections at various magnifications and length scales ranging from 1 μm to 1 mm). Such homogeneous dispersion was necessary to ensure repeatable property measurements with high fidelity and also to ensure our isotropic material for our subsequent thermal conductivity measurements.

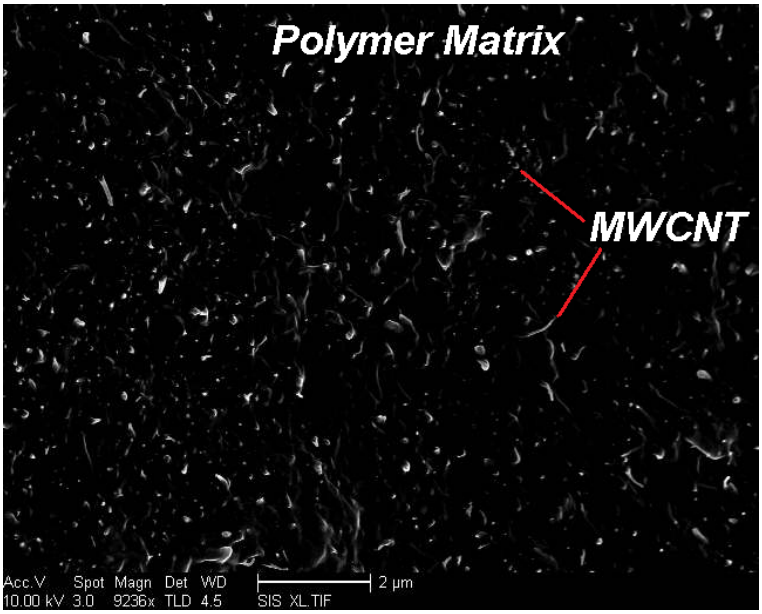

Figure 3.2: Scanning electron microscope (SEM) image indicating uniform dispersion of MWCNTs in polymer matrix.

We have used two varieties of MWCNTs with similar lengths (of $\sim$1.6 μm) with different diameters (45.0 $\pm$ 14.1 nm and 23.0 $\pm$ 6.3 nm) leading to aspect ratios of $\sim$ 35 and $\sim$ 70, respectively. Sonication of the nanotubes result in breakage of nanotube chains, and thus the geometrical parameters of the MWCNTs were measured using a Philips XL30 ESEM (environmental scanning electron microscope) to get accurate results after the sonication process. To get these measurements, 20-30 different MWCNTs were measured to get average value and the associated standard deviation. One such MWCNT measurement can be seen in figure 3.3. We noticed an almost 2 order reduction in the measured aspect ratio of the nanotubes with respect to supplier specs. We procure pre functionalized

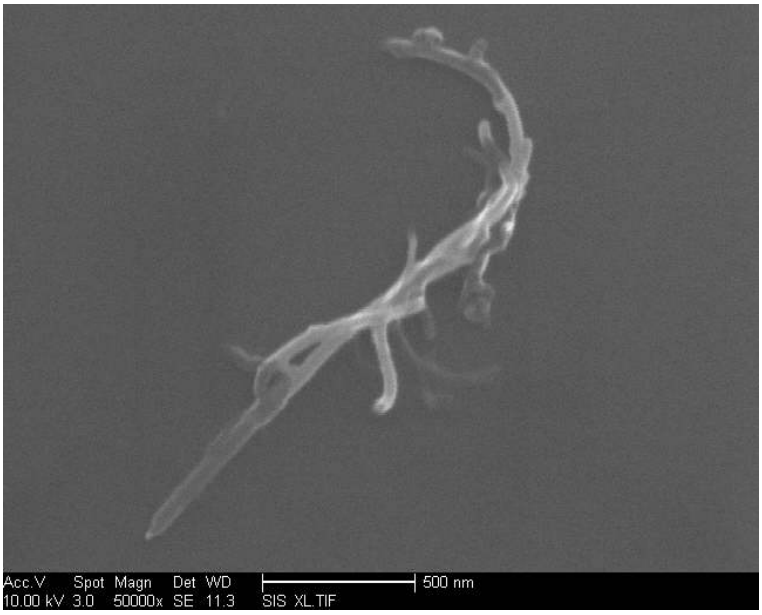

Figure 3.3: Scanning electron microscope (SEM) image used to measure length and diameter of sonicated single MWCNT

MWCNTs from www.cheaptubes.com for all our experiments.

3.2 Thermal conductivity increase

Using the steady state setup described in the previous chapter, we measured the thermal conductivity of both sets of composites. We made composites ranging from a 1 % volume fraction of MWCNTs all the way unto a 10 %. Higher volume fractions resulted in brittle samples. However, if the volume fractions could somehow be further increased, entangling of CNTs could also occur.

Percolation theory has been used extensively in the past to explore increase of electrical conductivity of composites with increasing CNT volume fraction. The rational here is the existence of conduction pathways formed by continuous chains of filler particles after crossing of a critical threshold of the filler volume fraction [15]. This critical volume fraction for percolation can be calculated by various methods. Original percolation theory was developed for spherical particles, with newer theory taking into account non-spherical - cylindrical filler particles. As per these theories, critical volume fraction for percolation for CNT like filler particles

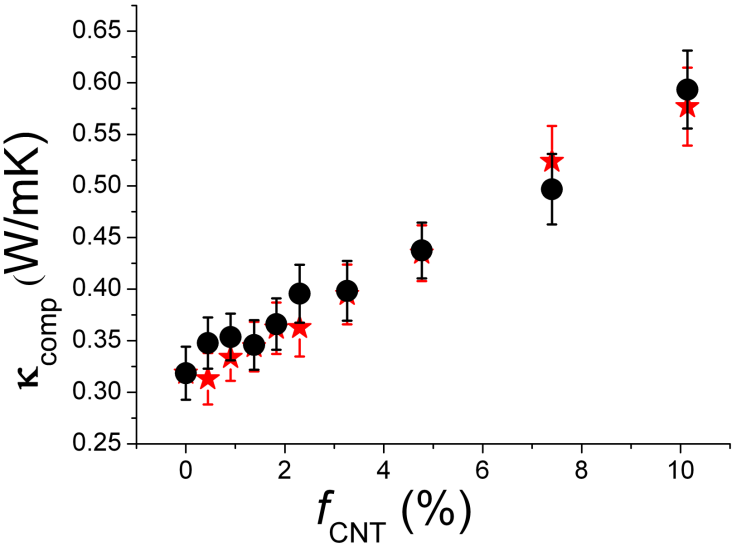

Figure 3.4: Experimentally measured values of κ_{comp} with increasing volume fraction of CNTs. Black circle symbols are for composites with MWCNTs of $A.R.$ = 35, while the red star are for composites with MWCNTs of $A.R.$ = 70.

with high Aspect Ratio is quite small compared to spherical particles. Thus we did originally expect to a see a percolation like behavior for our thermal conductivity measurements similar to what was observed previously for electrical conductivity measurements.

Table 3.1: Thermal conductivity of composite κ_{comp} for $A.R.$ = 35 and $A.R.$ = 70 MWCNT composites

Volume fraction of MWCNT (%)	κ_{comp} $A.R.$ = 35 (W/mK)	κ_{comp} $A.R.$ = 70 (W/mK)
0.44	0.34 ± 0.02	0.31 ± 0.02
0.90	0.35 ± 0.02	0.33 ± 0.02
1.38	0.34 ± 0.02	0.34 ± 0.02
1.83	0.36 ± 0.02	0.36 ± 0.02
2.30	0.38 ± 0.02	0.36 ± 0.02
3.26	0.38 ± 0.02	0.39 ± 0.03
4.77	0.44 ± 0.02	0.43 ± 0.03
7.40	0.50 ± 0.03	0.52 ± 0.04
10.14	0.59 ± 0.03	0.57 ± 0.04

Single walled nanotube (SWCNT)-epoxy composites were studied in Biercuk *et al.* [16], where the SWNTs were reported to be oriented randomly. An

increase in κ was the reported as a function of added SWNT weight content with a 125 % increase at 1 wt % SWNTs. The random orientation was thought to be the reason for the κ increase at a lower weight % compared to previous studies where the nanotubes were aligned perpendicular to the direction of current flow.

Initial understanding of such an increase was attempted by a simple mixing rule, using the thermal conductivities and volume fractions of the nanotubes (CNT) and the polymer (poly) matrix (*i.e.*, κ_{CNT}, κ_{poly} and f_{CNT}, f_{poly} respectively) through a relationship of the type: $\kappa_{comp} = \kappa_{CNT} \cdot f_{CNT} + \kappa_{poly} \cdot f_{poly}$. However, such a formulation suffers from the lack of precise knowledge of κ_{CNT} and also ignores possible filler-matrix interfacial contribution. The latter would preclude the use of simple mixture rules predicated on effective medium based approaches [17].

Using an excluded volume method [18], we calculated a critical volume fraction (f_{crit}) for percolation from:

$$f_{crit} = \frac{E[V_{ex}]N_{CNT}}{\frac{4}{3} + 2A.R. + \frac{1}{2}A.R.^2}\left(\frac{1}{6} + \frac{1}{4}A.R.\right) \tag{3.1}$$

For the derivation of equation above (explained in more detail in Pfeifer *et al.* [18]), we used an excluded volume percolation theory based model to estimate the theoretical critical volume percolation threshold, f_{crit}, of the CNTs, as a function of L. For this, we assumed that the i^{th} CNT has a volume, v_i, in a polymer/insulating matrix of unit volume. Now, if the percolation threshold corresponds to the connectivity of a number of CNTs ($=N_{CNT}$), then the odds of not selecting any CNT (corresponding to a point in the matrix) would be:

$$(1 - f_{crit}) = (1 - v_1)\left(\frac{1 - v_1 - v_2}{1 - v_1}\right)\left(\frac{1 - v_1 - v_2 - v_3}{1 - v_1 - v_2}\right)...$$

$$... \left(\frac{1 - v_1 - v_2 - ... - v_{N_{CNT}}}{1 - v_1 - v_2 - ... - v_{N_{CNT}-1}}\right) = 1 - N_{CNT}\sum_{i=1}^{N_{CNT}}\frac{v_i}{N_{CNT}} \tag{3.2}$$

Implying that $f_{crit} = N_{CNT}E[v]$. Here, $E[v]$ denotes the expected value or ensemble average of the CNT volume. It is to be noted that we have assumed that

the CNTs were impenetrable. We then use the identity $E[v] = \frac{E[V_{ex}]N_{CNT}}{E[V_{ex}]}\left(\frac{E[v]}{N_{CNT}}\right)$, where V_{ex} is defined as the excluded volume: the space circumscribed around the CNT by the center of another CNT, whereby both CNTs contact each other but do not overlap. For isotropically oriented, spherically capped stick like objects of diameter (d) and length (L), which we take to be akin to CNTs, $E[V_{ex}] = \frac{4\pi}{3}d^3 + 2\pi d^2 L + \frac{\pi}{2}dL^2$. Also, for the CNT modeled as a capped cylinder, $E[v] = \frac{\pi}{6}d^3 + \frac{\pi}{4}d^2 L$. For infinitely thin cylinders of deterministic length, Monte-Carlo simulations were used to estimate $E[V_{ex}]N_{CNT}$ of ~ 1.4 [19]. For a given aspect ratio ($A.R. = {}^{L}/_{d}$), the theoretical f_{crit} would then be as depicted in equation 3.2.

Consequently, we calculated $f_{crit} \sim 0.016$ ($= 1.6$ %) for samples $A.R.$ of 35 and for $f_{crit} \sim 0.009$ ($= 0.9$ %) for $A.R.$ of 70, were estimated. However, such thresholds are not apparent in the experimental observations of figure 3.4. We then sought to systematically understand the relative importance and contributions of the (a) polymer matrix, (b) polymer-CNT filler interface, and (c) the CNT geometry on κ_{comp}, to explain our findings.

While an increase in the thermal conductivity in the nanotube-polymer composites was observed in Bonnet *et al.* [20] a percolation threshold was not observed. Instead, after subtracting the contribution of the polymer matrix (PMMA in their case), the conductivity variation was fit to a scaling law to obtain a percolation like behavior. A major issue with this paper is that it does not again consider the influence of the interfacial resistance. A thermal conductivity contrast ratio of ten between the filler and the matrix was thought to be adequate for observing percolation related effects. Using similar methodology, we fit our data with $\Delta\kappa = \kappa_{measured}$ - $\kappa_{poly} \cdot (1 - f)$ against reduced volume fraction $(f - f_{crit})/(1 - f_{crit})$. When we fit this data with a percolation equation $\Delta\kappa = \kappa_o[(f - f_{crit})/(1 - f_{crit}]^{\beta}$, we get value for $\kappa_o \sim$ 1.3 W/mK. This value is implied to be for the carbon nanotubes, and is orders of magnitude smaller than what is commonly accepted.

We believe the lack of percolation is due to the inherently large interface thermal resistance between MWCNT and the RET polymer. It has also been shown from molecular dynamics simulation[21], that CNT-CNT interface is really ineffective for transport of heat due to the really small contact area. It was

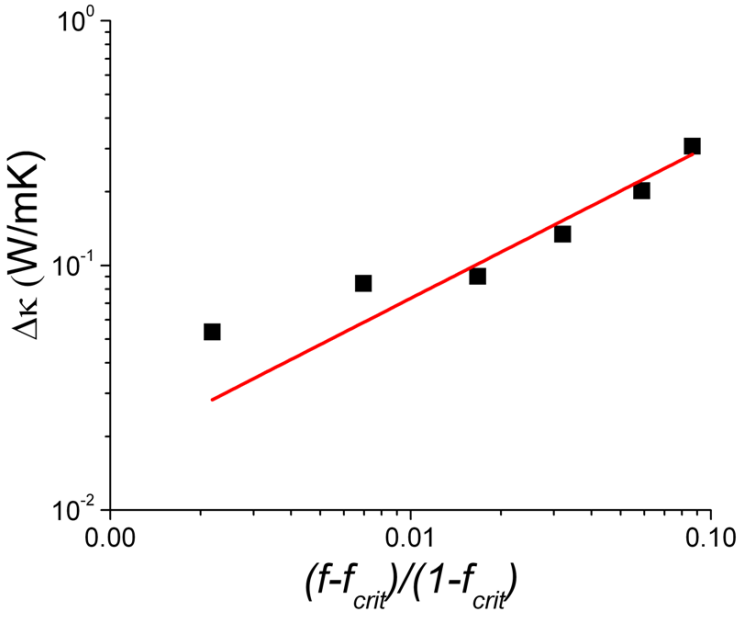

Figure 3.5: Fitting with Bonnet model for subtracted thermal conductivity enhancement of CNT in the composite.

also previously been concluded through theoretical analysis (based on the finite element method: FEM and molecular dynamics) that the low thermal conductivity (κ) contrast (of less than 10^4) between the matrix and the filler precludes a strong percolation threshold effect [21]. Thus there is an degradation in the effective thermal conductivities of these networks. A linear variation of the thermal conductivity with volume fraction was consequently predicted based on effective medium theory [22].

From multiple-scattering approach of Nan [23], Effective thermal conductivity for a composite medium is given by $\kappa = \kappa^o + \kappa'(r)$, where κ^o denotes the constant part of the homogenous base medium while $\kappa'(r)$ denotes the arbitrary fluctuating part. Using Green function G [24] for the homogenous composite medium and the tradition matrix T for the entire composite medium, a rigorous solution for the temperature gradient distribution can be obtained. The resulting effective thermal conductivity can be expressed as $\kappa = \kappa^o + < T > (I + < GT >)^{-1}$. Here I is the unit tensor and <> denotes spatial averaging [25]. More details about this approach can be found in references.[23, 24, 25]

Interface resistance (Kapitza Resistance) is the inverse of interface thermal conductance [26] and is defined by

$$q_{interface} = -G\Delta T \tag{3.3}$$

Here G is the interface conductance, while ΔT is the temperature drop at the interface.

Huxtable et al.[27] have measured a Kapitza Resistance of CNT matrix to be $8.3 \cdot 10^{-8}\ m^2K/W$. This value of thermal resistance is of the same order of magnitude as of the bulk polymer. We have subsequently tried fitting our thermal conductivity data with a Maxwell-Garnet-type effective medium approach [28].

Kapitza radius a_k is defined by

$$a_k = R_k * \kappa_{poly} \tag{3.4}$$

Here R_k is the Kapitza Resistance, and κ_{poly} is the thermal conductivity of the polymer matrix, RET in our case.

We modeled the CNT-polymer matrix interface, through a unit cell as shown in Figure 3.6. Such an approach assumes that the environment around each CNT in the composite is substantially identical and may be accurate with compositions outside the percolation threshold volume fraction [22]. We also assume no heat storage in the composite or interface, a finite interfacial layer thickness, heat flux continuity across the interface, and a finite temperature discontinuity proportional to the heat flux across the interface. We employ a cylindrically shaped unit CNT, with κ_t^{cell} and κ_l^{cell} as the equivalent thermal conductivity values along transverse (cross-sectional) and longitudinal axes. The *net* thermal resistance along this unit cell was computed through the addition of individual thermal resistances of the (i) two interfacial layers (R_{int}) on either end, together with that from the (ii) CNT, ($= {}^{L}/_{\kappa_{CNT}}$ or ${}^{d}/_{\kappa_{CNT}}$), and yields for the equivalent thermal conductivity:

$$\kappa_t^{cell} = \frac{\kappa_{CNT}}{1 + \frac{2R_{int}}{d}\kappa_{CNT}} \tag{3.5}$$

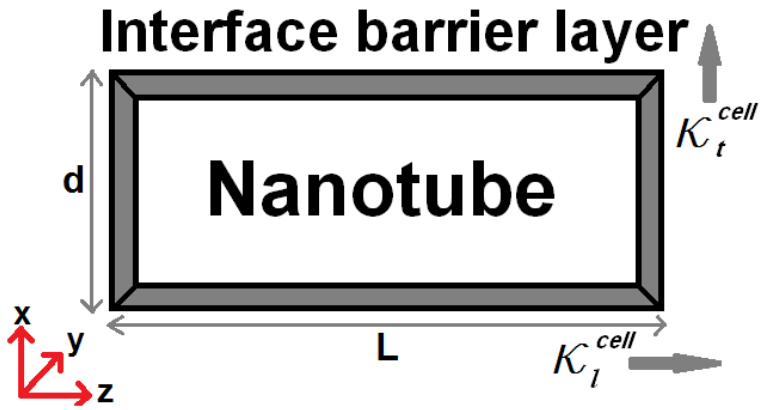

Figure 3.6: A unit cell of a CNT with surrounding interface layer was used as a constituent to model the nanotube - polymer composite.

$$\kappa_l^{cell} = \frac{\kappa_{CNT}}{1 + \frac{2R_{int}}{L}\kappa_{CNT}} \tag{3.6}$$

Subsequently, by following the approach of Nan *et al.* [24, 25], who also assumed such an effective medium based theory, the κ_{comp} relative to the polymer matrix conductivity (κ_{poly}) was expressed using:

$$\frac{\kappa_{comp}}{\kappa_{poly}} = \frac{3 + f(\beta_x + \beta_z)}{3 - f\beta_x} \tag{3.7}$$

where,

$$\beta_x (= \beta_y) = \frac{2(\kappa_t^{cell} - \kappa_{poly})}{\kappa_t^{cell} + \kappa_{poly}} \tag{3.8}$$

$$\beta_z = \frac{\kappa_l^{cell}}{\kappa_{poly}} - 1 \tag{3.9}$$

The data shown in Figure 3.7 & 3.8 was fitted using equations 3.5 to 3.9 and yielded an R_{int} of $9 \cdot 10^{-8}$ m^2K/W. Such a value was comparable to the 8.3 $\cdot$ 10^{-8} m^2K/W, estimated for single walled CNTs encased in cylindrical micelles of sodium dodecyl sulphate surfactant [27, 29] and to that calculated for SWCNTs through molecular dynamics based simulations [30]. The R_{int} could then mask/curtail the connectivity of the CNTs and result in our not seeing high values

of thermal conductivity enhancements for the composites. To check this influence, we fitted the model with different values of κ_{CNT}, varying it from 50 W/mK to 500 W/mK. We see relative insensitivity of the experimental fits (in figure 3.7 & 3.8) with this change, which is quite unexpected intuitively. However, we observed maximal r^2 values, of around 0.97 and 0.98 respectively for $A.R.$ 35 and $A.R.$ 70 samples with a $\kappa_{CNT} = 500$ W/mK. This value for κ_{CNT} is comparable to what is generally observed in literature for MWCNTs. (Put reference) Further increasing κ_{CNT} has negligible effect.

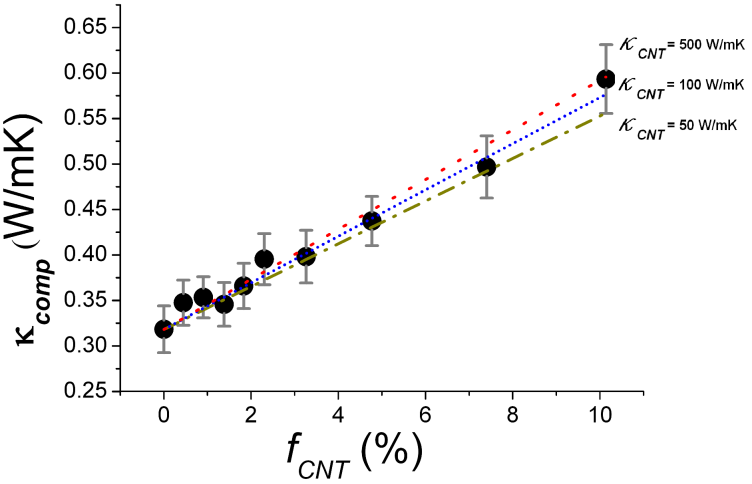

Figure 3.7: Modeling κ_{comp}, using κ_{CNT} as a fitting parameter. Black circle symbols indicate experimental values for composites constituted of MWCNTs with an average $A.R.$ of 35.

Given the close correspondence of the determined R_{int} to previous experiments and the reasonable value of κ_{CNT} , we can conclude that our approach can be used to study thermal transport behavior in such nanotube-polymer composites. However, the implicit assumption of an uniform environment for all the constituent CNTs could hold only up to a certain range of CNT filler volume fraction [31] and will not be applicable for higher volume fractions which would result in entangling of the filler particles, and thus more complex interactions between the filler and polymer matrix.

Subsequently, we wish to further understand the role of the interface and the interfacial resistance. We propose a circuit model for thermal transport through

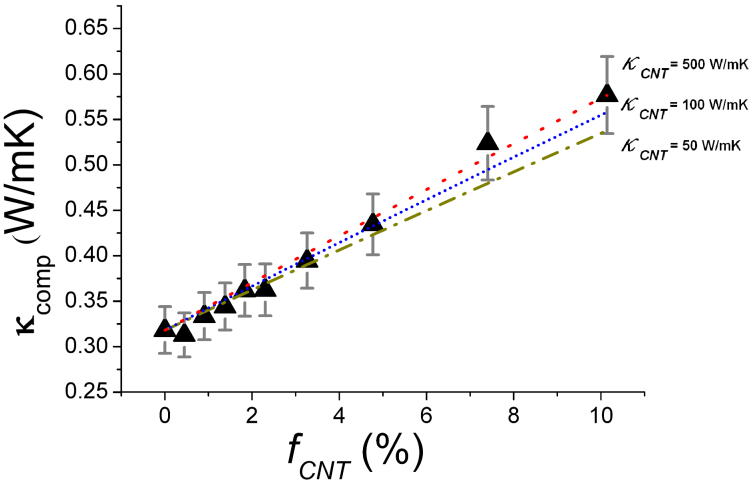

Figure 3.8: Modeling κ_{comp}, using κ_{CNT} as a fitting parameter. Black triangle symbols indicate experimental values for composites constituted of MWCNTs with an average $A.R.$ of 70.

the nanotube-polymer composite, as shown in figure 3.9 similar to an electrical circuit. For such composites, we can assume two parallel paths: one through the interface/CNT/interface and another through the polymer matrix. The thermal resistance per unit area in the former path (R_{total}) is the sum of the thermal resistances of CNT (R_{CNT}) and the two interfacial resistances (R_{int}). For the polymer matrix (*i.e.*, R_{poly}) we calculate the thermal resistance (l / κ)to be $\sim 5 \cdot 10^{-6}$ m^2K/W computed over the length of the nanotube. To compare the two thermal resistances, we change κ_{CNT} from 10 to 1000 W/mK and explore its effect on R_{total}/R_{int} ratio. As seen in figure 3.10, we that this ratio tends to one, after a κ_{CNT} of $\sim$ 100 W/mK. Further increase of κ_{CNT} does not have any effect in the enhancement of κ_{comp} as the interface resistance is much more dominant and the CNT contribution is effectively cut off.

From our data measurements for two sets of composites with different $A.R.$, it originally seemed the increase of composite thermal conductivity was independent of the $A.R.$ which was something not previously expected. To further explore this, we use the EMA model and calculate κ_{comp} by changing the $A.R.$. This can be done by two distinct ways, first we keep the diameter (d) constant and change length (l) of the nanotubes, which would result in increase of κ_l^{cell}, and subse-

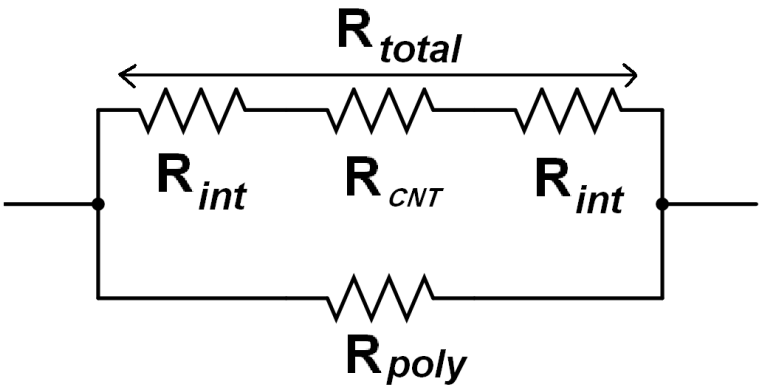

Figure 3.9: Equivalent circuit model for thermal transport in a nanotube-polymer composite. The top branch indicates the two interfaces in series with a CNT, while the bottom branch models heat flow through the polymer matrix.

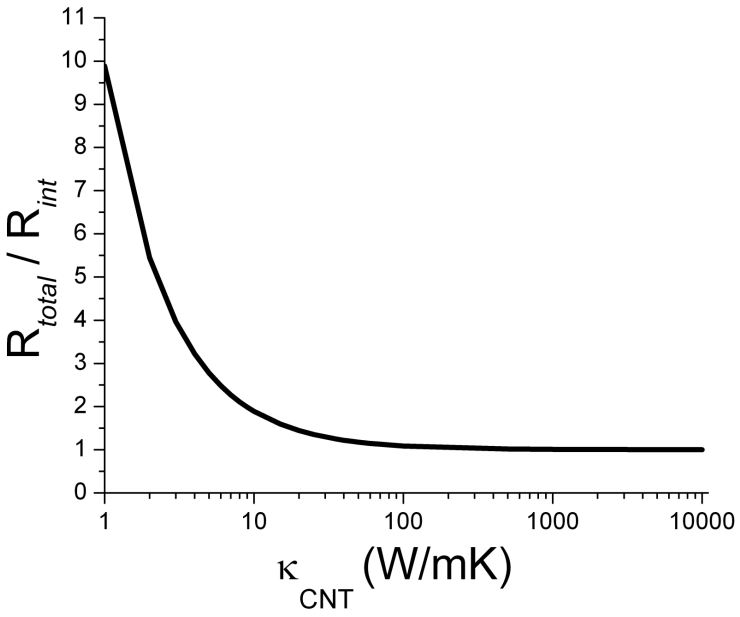

Figure 3.10: Ratio of the thermal resistance from the nanotube and two interfaces: (R_{total}) to the interfacial resistance, (R_{int}), as a function of the intrinsic thermal conductivity of the CNT: κ_{CNT}.

quently we keep l constant and change d, which would result in increase of κ_t^{cell}. Increase of either of these quantitates would result in increase of κ_{comp}. Comparing the modeled κ values in figures 3.11 and 3.12, we see that increasing the $A.R.$ of composites by increasing the length of MWCNTs has a greater effect on the increase in the κ_{comp} than by changing the diameter. This can also be attributed to the length being at least two orders of magnitude bigger than the diameter. Thus comparing the experimental results to the modeled lines in figures 3.12, we see that a diameter induced variation of the $A.R.$ had less of an influence on the κ_{comp} variation, in accordance with experiments. Consequently, the experimentally observed κ_{comp} would be more related to a diameter variation as lengths of MWCNTs we use for our experiments is same in both the cases.

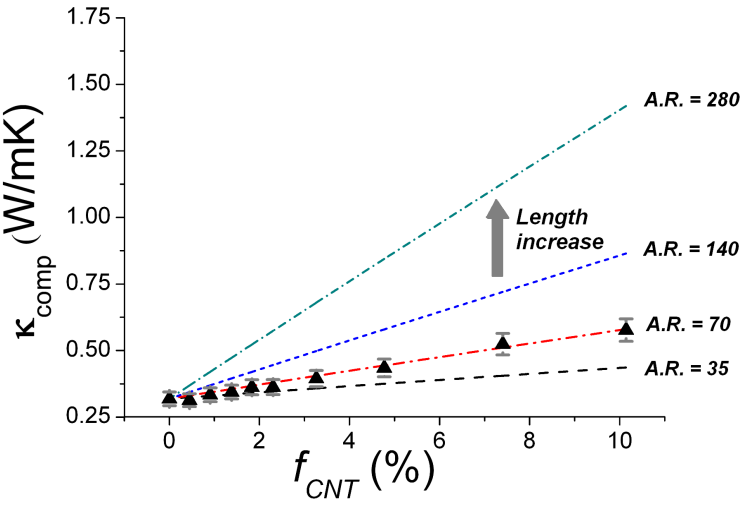

Figure 3.11: Modeled κ_{comp} increase, showing effect of increasing length, L of MWCNT (d is constant). Black triangle symbols indicate experimental data for composites with constituent MWCNT fillers of average $A.R.$ of 70.

Lastly to be able to make composites with higher thermal conductivity, we will need nanotubes with longer length.

Most of the work described in this chapter has been adopted from Kapadia, R. S., Louie, B. M., Bandaru, P. R., "The influence of carbon nanotube aspect ratio on thermal conductivity enhancement in nanotube-polymer composites", *Journal of Heat Transfer*, v.136, 011303, 2013.

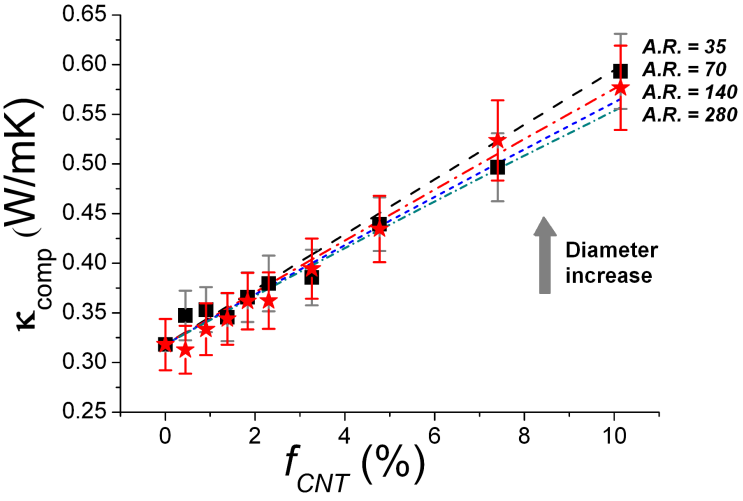

Figure 3.12: Modeled κ_{comp} increase showing effect of increasing d of MWCNT (L is constant). Black symbols are for composites with MWCNTs of $A.R. = 35$, while red symbols are for composites with MWCNTs of $A.R.$ of 70, both denoting experimental values

4 Fourier Law for Heat Conduction and its application for heat flux concentration

Fourier Law governs heat conduction. For a steady state condition, as per Fourier law, heat flux (q) is directly proportional to thermal conductivity (κ) and inversely proportional to the length of the conductor (dx) for a constant Temperature gradient applied (dT)

$$q = -\kappa \frac{dT}{dx} \tag{4.1}$$

From this relation, we see that heat flux can be concentrated by changing geometry (dx) as well as thermal conductivity (κ).

4.1 Analytical flux concentration

Based on the Fourier law, we have tried to explore analytically how heat flux can be concentrated.

We start with exploring the effect of heat flux concentration by changing the thermal conductivity. We take a structure with 3 layers shown in figure 4.1. We assume thermal conductivity of layer 1 = 1 W/mK, and for layer 2 = 2 W/mK. Subsequently we change the thermal conductivity of layer 3, changing it from 4 W/mK to 16 W/mK. We keep the temperature on edge of layer 1 = 350 K, and temperature on edge of layer 2 & 3 to be 300 K. Based on Fourier law, we would

expect the heat flux in layer 3 to be higher as it is directly proportional to the thermal conductivity ratio of layer 3 to layer 2. We take $\kappa_1 = 1$ W/mK.

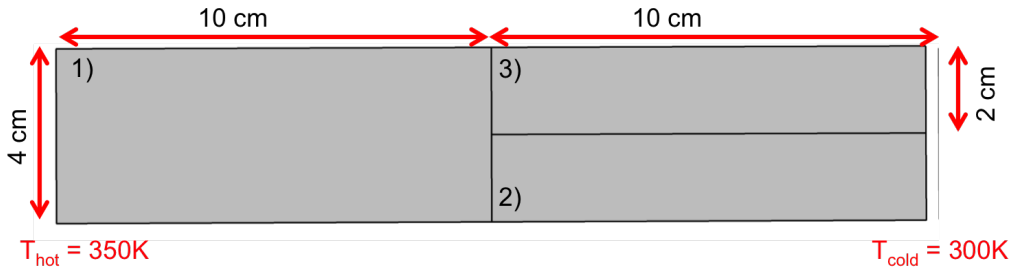

Figure 4.1: Schematic of setup to explore heat flux concentration by Fourier Law

Table 4.1: Heat flux in layers with changing thermal conductivity

κ_2 (W/mK)	κ_3 (W/mK)	Theoretical q_3 / $q_2 = \kappa_3$ / κ_2	Simulated q_3 / q_2
2.0	4.0	2.0	1.99
2.0	8.0	4.0	3.99
2.0	16.0	2.0	7.96

Taking this further, we explore the effect of heat flux concentration by changing the geometry by changing the length of the conductor. We change the length of layer 3, and make it half the length of layer 2. As heat flux is inversely proportional to the length of the conductor, we would expect flux in layer 3 to be double that in layer 2. We take $\kappa_1 = 1$ W/mK and notice from simulation results that q_3 / $q_2 = L_2$ / $L_3 = 2$.

Further we probe the effect of reduction in length on flux concentration, by changing the length of material 3 to be 0.5 times the length of material 2, keeping thermal conductivity of material 2 to be two times that of material 3. We notice q_3 / $q_2 = 3.96$, which compares to analytically predicted q_3 / $q_2 = (L_2$ / $L_3)$ * (κ_3 / $\kappa_2) = 4.0$.

4.2 Experimental flux concentration

Based on the analytical flux concentration as discussed in the earlier section, we explore experimental measurements to confirm this effect. We pick polymers with distinct thermal conductivity values to make geometries with 2 layers. As can be seen in the figure we use teflon to make the hot side block, we measure the thermal conductivity of teflon using our steady state setup and get a value 0.23 W/mK which compares with literature [11]. For the two blocks being subjected to cold side sink, we pick High Density Polyethylene (HDPE) and Acrylic. Thermal conductivity of HDPE ~ 0.45 W/mK, while that of Acrylic is ~ 0.20 W/mK. Thus from Fourier law, we expect the heat flux in HDPE to be more than two times the flux in Acrylic.

4.2.1 Experimental Setup

Experimental measurement of heat flux is difficult, as use of heat flux sensors would add extra thermal resistance to the setup and give inaccurate measurements. Narayana and Sato [32] have used a contact less method for measurement of heat flux using an Infra Red Camera coupled with COMSOL simulations. Using an I.R. camera, we can measure temperature profile on the surface of our setup. Subsequently we can compare this measured temperature profiles with those generated by COMSOL simulations. For same boundary conditions, we can assume that heat flux in the experimental setup is similar to those in simulations if temperature profiles are similar. Thus we can then extract the corresponding heat flux values for the simulations.

Using IR camera requires a constant high emissivity value of the surface being measured to ensure minimum errors. Thus we use lampblack paint to paint the surfaces being measured. By ensuring a thin layer of paint on the surface of our polymers, we can assume negligible conductive flux along the surface of the paint, and take the temperature being measured at the surface of the paint to be same as the temperature of the polymer underneath. Lampblack paint has an emissivity value of ~ 0.95, which is what we enter in the camera software to deduce

the temperature values. To ensure minimum radiative losses from other surfaces of the setup, we paint them with a really low emissivity paint LO/MIT-II from Solec Energy Corp. This paint has emissivity values of less than 0.2 when applied to polymers using an airbrush. We also use radiation shields, which are kept quite close, $\sim$ 5 mm to the setup. These shields are also subjected to same hot and cold side temperatures, thus they act like a guarded hot plate and result in minimum radiative and convective losses. We estimate radiative and convective losses to be at the most $\sim$ 10 % for our complete setup. Using COMSOL, we run simulations by assuming these losses and estimate minimal disturbance in the temperature profiles being generated on the surface of the setup.

All our experiments are performed at constant temperature boundary conditions. We use a hot plate for the hot side, but noticed a non-uniform temperature surface being setup on the top surface. To ensure a uniform hot temperature, we keep a block of Copper on the hot plate to act as the constant hot temperature surface. Copper with really high thermal conductivity ensures minimal variation in the surface temperature. We confirm this by using the IR Camera.

Setting a uniform cold temperature proved to be trickier. Initially we tried to use ice boxes on the cold side as done by Narayana and Sato. [32] As polymers have low specific heat, reaching a steady state temperature conditions takes a longer period of time. Using ice boxes proved to be cumbersome as the ice would start melting and we would need to change the box every 10 minutes to ensure constant low temperature. Repeated changing of the ice boxes would result in a non-uniform cold temperature, and could result in inaccurate results. Thus we designed and fabricated a custom cold plate setup for this task. We use a Peltier cooler as the cold temperature generating device for our setup. To ensure constant sinking of heat from the Peltier cooler, we used a liquid cooling setup generally used for high end computers from Corsair. This setup uses water with a proprietary additives and acts as an excellent sink for our setup. We use copper plates on both sides of the Peltier cooler to ensure uniform temperature. By controlling the current being supplied to the Peltier cooler, we were able to maintain a constant temperature from 5 °C to 20 °C. We use Arctic Silver 5 in between all contact

surfaces to ensure minimal thermal contact resistances.

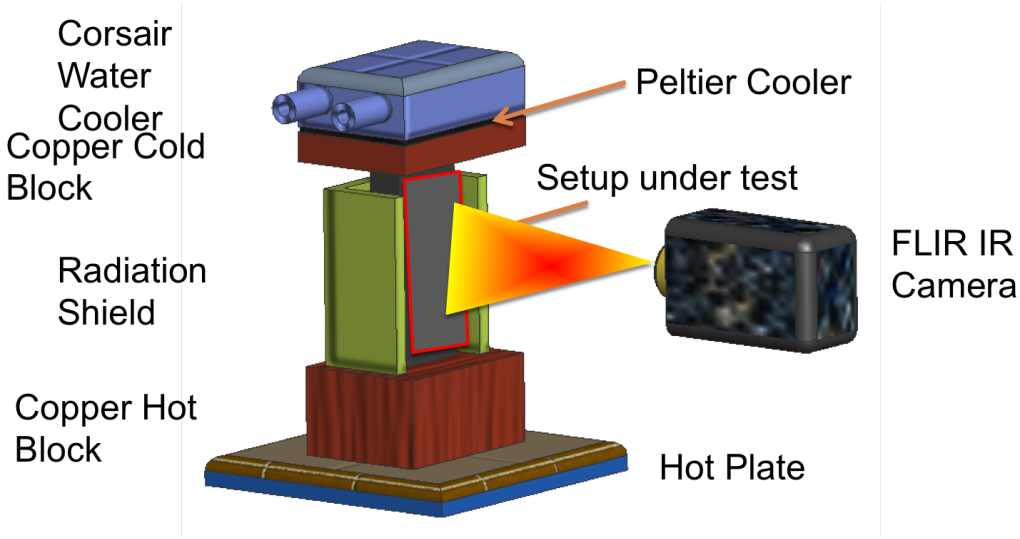

Figure 4.2: Schematic of experimental setup showing an IR camera being used to measure temperature profiles of an experimental setup

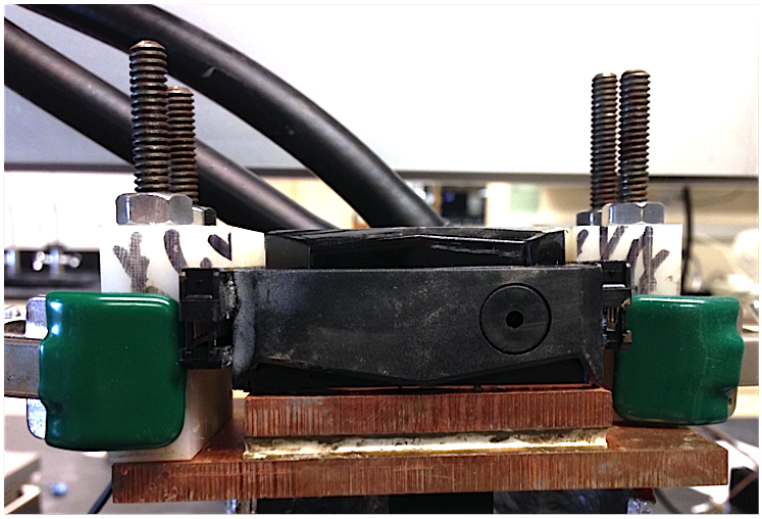

Figure 4.3: Custom cold plate setup designed and fabricated using a Peltier cooler and a computer water cooler

4.2.2 Experimental Results

Using the setup described in detail in the previous section, we measure the temperature profiles on surface of our setup at different hot and cold temperature

Figure 4.4: Experimental setup showing an FLIR A320 camera being used to measure temperature profiles of an experimental setup

temperatures. We compare them with ones in simulation and notice similar profiles in our experiments with those predicted by the simulations. This would mean, that heat flux in the experiments are similar to ones we can extract from the simulation. From our simulations, we know that heat flux in the HDPE layer is ~ 2 times the heat flux in the Acrylic layer as predicted by Fourier law. We plot the flux across the Teflon cross-section as well as a cross-section in the Acrylic - HDPE blocks near the cold temperature side, and notice the flux as predicted in figure 4.7.

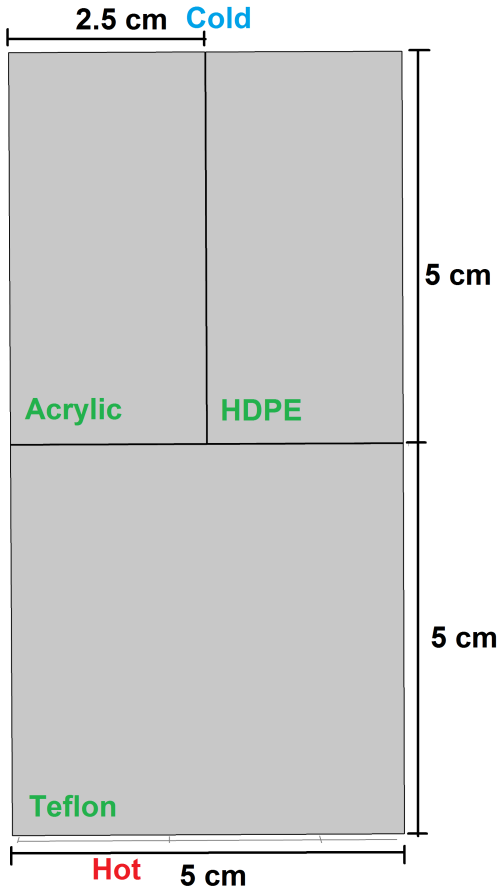

Figure 4.5: Experimental setup for observing effect of heat flux concentration using HDPE and Acrylic blocks

Thus we see from these experiments that we can use materials with different thermal conductivity to concentrate heat.

Some material from this chapter is currently being prepared for submission for publication. The dissertation author, Rahul S. Kapadia was the primary

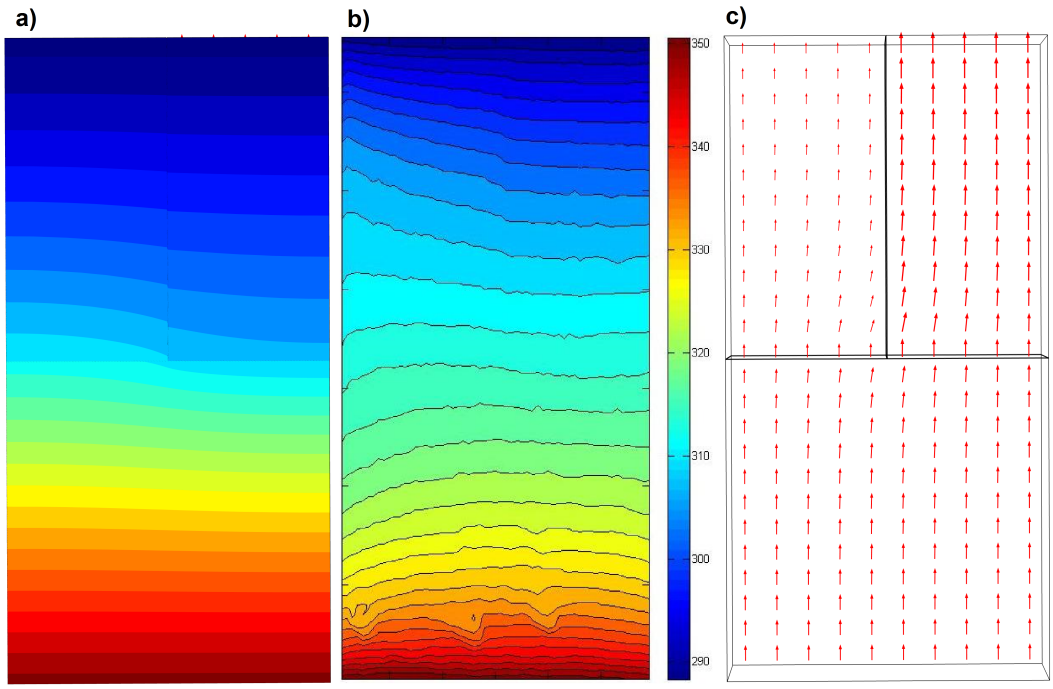

Figure 4.6: Comparison of Experimentally measured temperature profile with simulations. Figure a) shows temperature contours in simulation, figure b) shows experimentally measured temperature contours while figure c) shows the heat flux in simulations

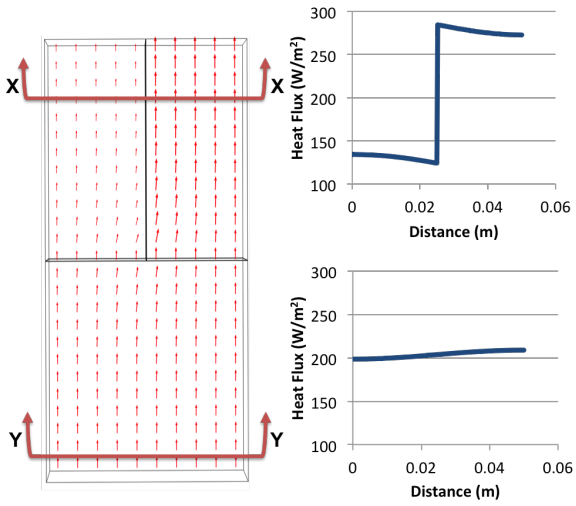

Figure 4.7: Heat flux plotted in Teflon block at Y-Y cross section and heat flux plotted in Acrylic - HDPE block at X-X cross-section

investigator and author of this material.

5 Tangent Law for Heat Conduction

Tan and Holland have previously derived a analytical relation for refraction for heat conduction through an interface [4]. This relation is analogues to the Snell's Law which pertains to wave refraction when it travels from one medium to another. The heat flux vectors can be considered to be heat rays and they travel in a direction perpendicular to the isothermal lines, which is predicted by the Fourier Law.

To derive this relation, we can consider a heat flux vector traveling from one material to another as shown in figure 5.1. We take an assumption of steady state, and also absence of any interfacial resistance (perfect interfacial contact) and any heat sources or sinks at the interface boundary. This would ensure a continuity of temperature across the interface, and corresponding absence of any temperature slip type conditions. In the figure, we take two materials 1 & 2, with thermal conductivities of κ_1 & κ_2 respectively.

From this temperature continuity, we can hypothesize that

$$\mid \nabla T \mid_1 sin\theta_1 = \mid \nabla T \mid_2 sin\theta_2 \tag{5.1}$$

Due to the absence of any heat sources or sinks at the boundary interface

$$\kappa_1 \mid \nabla T \mid_1 cos\theta_1 = \kappa_2 \mid \nabla T \mid_2 cos\theta_2 \tag{5.2}$$

Dividing equation 5.1 by equation 5.2, we get

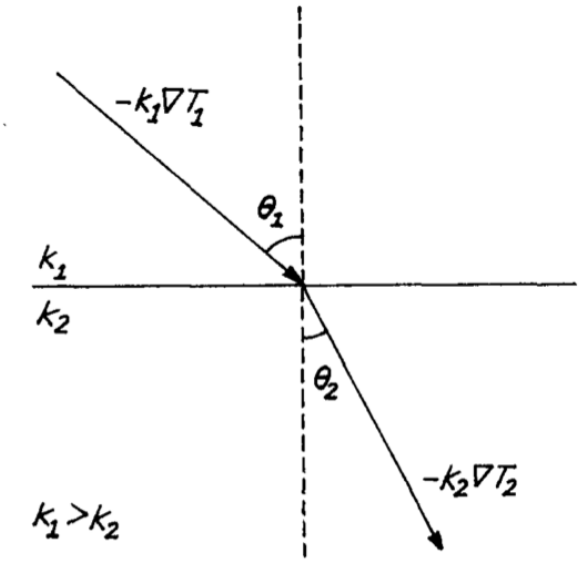

Figure 5.1: Refraction of heat flux vector at interface of 2 materials [4]

$$\frac{tan\theta_1}{\kappa_1} = \frac{tan\theta_2}{\kappa_2} \tag{5.3}$$

This equation denotes the tangent law of refraction for heat conduction. If we take an analogy with electrical current, and propose a quantity of thermal resistivity ($\rho = 1/\kappa$), then we can come up with the following form of equation;

$$\rho_1 tan\theta_1 = \rho_2 tan\theta_2 \tag{5.4}$$

This form of equation is analogues to the Snell's law. Here tangent is corresponding to the sine function used in the Snell's law in optics.

5.1 Validation of Tangent law through simulations

To check the validity of the Tangent Law of heat refraction, we performed multiple simulations in COMSOL. We take a structure similar to shown in figure below. Taking material 1 to be Steel with $\kappa = 43$ W/mK, material 2 to be Copper

with $\kappa = 401$ W/mK, and material 3 to be Nickel with $\kappa = 91$ W/mK, we perform simulations with constant temperature boundary condition as denoted. Taking $T_{hot} = 350$ K & $T_{cold} = 300$ K, we obtain the temperature iso-contours and heat flux profile as shown below.

Subsequently we measure the incident and the refracted angle of heat flux vectors at all three interface boundaries; Steel - Copper, Steel - Nickel and Nickel - Copper. We compare the measured value of refracted angle with the one predicted by the Tangent law and find the values quite close and within 5% for all three cases.

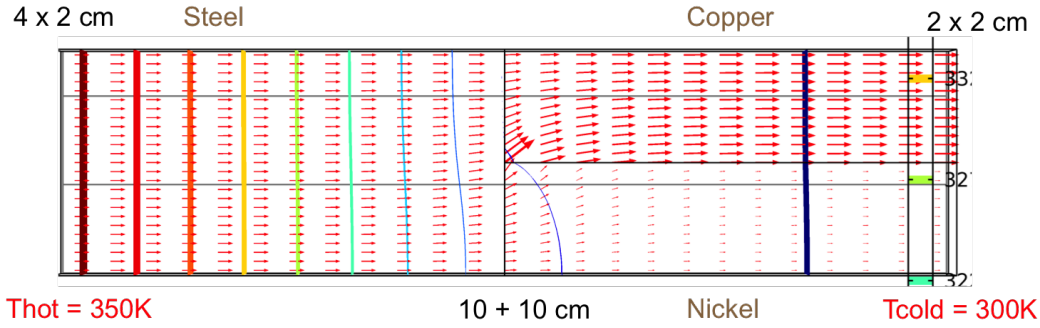

Figure 5.2: Temperature profile in Comsol simulation for measuring angle of refraction

Table 5.1: Measured and Calculated angle of Refraction in simulations

Interface	Incident Angle (°)	Calculated Refraction Angle (°)	Measured Refraction Angle (°)
Steel - Copper	4	33	31
Steel - Nickel	26	46	45
Nickel - Copper	22	61	64

We have also performed simulations by using different materials and do see similar trends in the measured and calculated angle of refraction for all cases.

5.2 Experimental validation of Tangent law

We did extensive literature survey and noticed a complete absence of experimental validation of the tangent law of heat refraction. Thus did further explorations to validate it through our experiments.

Temperature iso-contours are obtained from one of our Polymer experiments, discussed extensively in the previous chapter and is shown below.

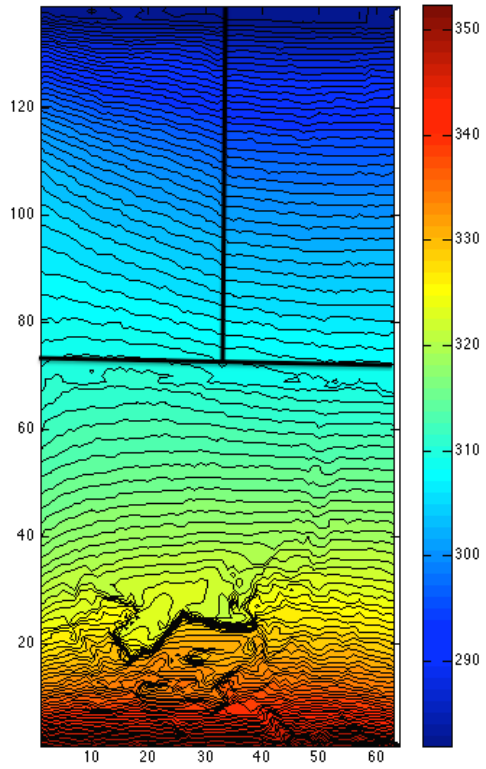

Figure 5.3: Temperature profile obtained by IR camera with T_{hot} = 351 K & T_{cold} = 282 K

We measured the incident and refracted angles at the three different points along the Acrylic- HDPE Interface, using experimentally measured thermal conductivity of HDPE $\sim$ 0.45 W/mK, and Acrylic being $\sim$ 0.20 W/mK.

As can be seen from the values we measured, they compare quite well with

Table 5.2: Measured and Calculated angle of Refraction for Acrylic and HDPE experimental measurements

Case	Incident Angle (°)	Calculated Refraction Angle (°)	Measured Refraction Angle (°)
1	73	82	76
2	67	79	73
3	61	76	74

the calculated values and are within 8 % for all three cases. These measurements prove the experimental validation of the Tangent law for heat refraction.

Some material from this chapter is currently being prepared for submission for publication. The dissertation author, Rahul S. Kapadia was the primary investigator and author of this material.

6 Analytical study for heat flux concentration

We try to make structures similar to an optical convex lens. As seen in figure below, an optical convex lens focuses light at a focal point at some distance (f). We make an analogous structure to concentrate conductive heat flux based on concentrations we saw in the previous chapter. We make a structure with radius of curvature R on one edge, and take a straight / vertical edge ($R \sim \infty$) on the other. This structure concentrates heat at the center of the curved edge. Conductive heat flux follows the path of least thermal resistance, similar to how current follows the path of least electrical resistance. Thermal resistance per unit area is given by l/κ, where l is length of conductive path and κ is the thermal conductivity. Reducing the length (l) of the structure at the center results in lower thermal resistance for the respective path, and thus heat flux is concentrated at the center.

$$q = -\kappa \frac{dT}{dx} \tag{6.1}$$

6.1 Circular Radius lens and its analogy with a straight edged lens

6.1.1 Lens with constant thermal conductivity

The effective ability of these structures to concentrate heat flux can be evaluated by simulating structures with a straight edge and then comparing them with ones with a curved surface with a specific radius. For our simulations, we

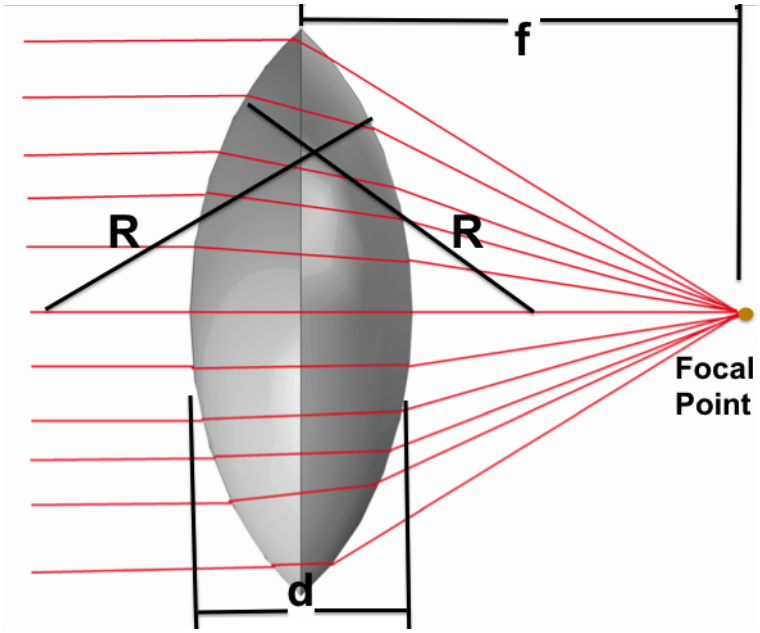

Figure 6.1: Convex lens geometry showing focusing of light at a focal distance f

define our structure with following variables, H (height of block), θ (angle of bending) and W (width of lens). These 3 variables can be compared to H, R (radius of curvature) and W for our curved lens structure. For comparisons, we perform a simulation taking a lens structure with $H = 3$ cm, $W = 2$ cm and $\theta = 45$ °. Simulations are performed with constant temperature boundary conditions applied to the edges of the setup so as to explore effects of heat flux with respect to thermal conductivity and length of the conductor. To ensure that the lens structure is being subjected to uniform flux, we keep a block of acrylic between the hot temperature boundary and the lens. This ensures that the heat flux lines at the lens structure are parallel, which is analogous to a collimated beam of light. The other edge of the lens is kept at a constant cold temperature. We performed simulations with $T_{hot} = 360$ K and $T_{cold} = 290$ K. Under these temperature conditions, the heat flux profile at the edge of the lens can be seen in the figure below. To measure concentration effects, we measure average heat flux at the edge and center of the lens structure (q_{edge} and q_{center}). The values are averaged over a 1 mm distance to reduce edge / mesh effects. Using these values we see a concentration ratio = q_{center}r / $q_{edge} \sim 100$ for this specific geometry.

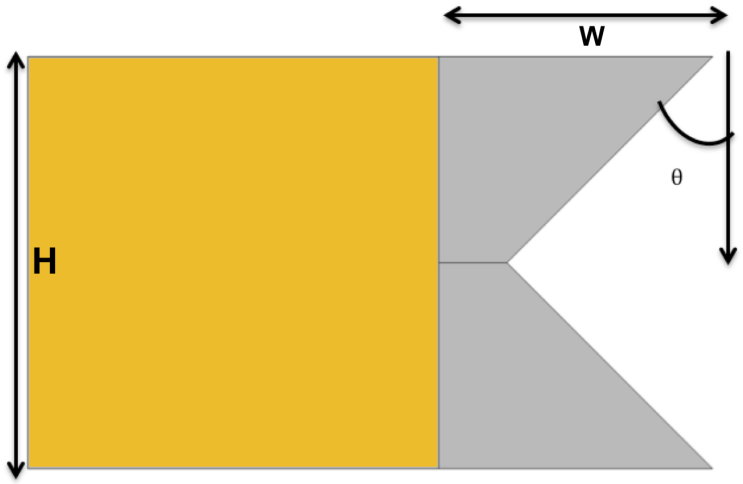

Figure 6.2: Straight edge structure for concentrating heat flux at center, shown with geometric parameters

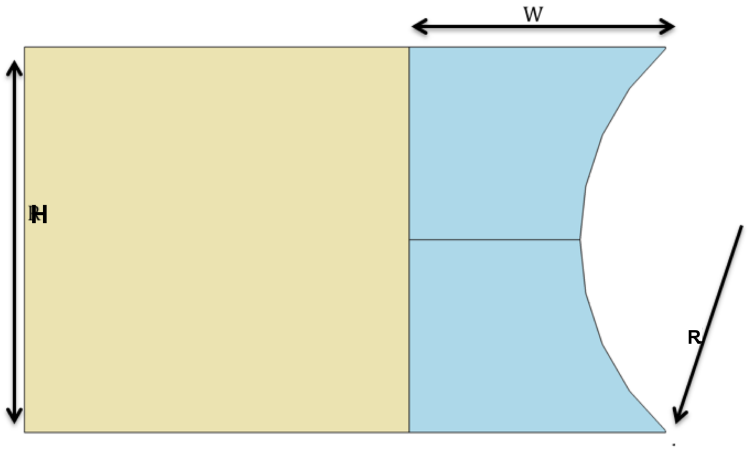

Figure 6.3: Curved edge structure for concentrating heat flux at center, shown with geometric parameters

Using a curved lens structure, we see similar concentration at the center. For example, there is a concentration ratio of ~ 99, when R = 1.76 cm. Keeping the same values for W and L, the ratio varies from 6090 to 23, when R is varied from 1.5 cm to 2 cm. Thus we can conclude that a curved lens structure with R = 1.76 can be considered to be similar to our structure with straight edge. From a similar approach, we can choose a circular geometry for a specific concentration ratio, and then find a corresponding straight edge structure to get similar effect.

6.1.2 Lens with changing thermal conductivity

In the first part, we have explored heat flux concentration using geometric parameters. Thermal resistance is inversely proportional to the thermal conductivity of material. Thus increasing thermal conductivity would result in lower thermal resistance, and this effect can also be used to concentrate heat flux. In the structure shown below, we take a rectangular structure, but change the thermal conductivity linearly as we go from center to edge. Taking $\kappa_{center} = 4$ W/mK and $\kappa_{edge} = 0.5$ W/mK, we change the thermal conductivity linearly for the material between the two extremes. Plotting the heat flux at the edge of the structure, we see the concentration ratio q_{center} / $q_{edge} = 7.85$ which compares to κ_{center} / $\kappa_{edge} = 8$. This ratio proves that heat flux does get concentrated based on ratio of thermal resistance as predicted by Fourier Law if the length is kept constant.

6.1.3 Lens with changing geometry and thermal conductivity

Subsequently we can combine the effect of thermal conductivity and geometry to get a coupled heat concentration effect. In this case we have a structure as shown in figure 6.3 with R = 2 cm, but instead of the lens being made of an isotropic material, we assume a material with changing thermal conductivity. We keep the thermal conductivity highest at the center, and lowest at the side. We simulate two different cases of the conductivity variation, linear and exponential. We do see for both cases the heat conductivity concentration at the center is much

higher than what is observed for just geometrical effect. Flux concentration for isotropic material is ~ 23, while for linear and exponential conductivity increase it is ~ 87. The similarity in the resulting concentration ratio for the linear and exponential thermal conductivity variation stems from the fact that there is lower flux at the sides in case of linear conductivity, making the concentration ratio similar to what is obtained by exponential case, which has a higher absolute value of flux at the center.

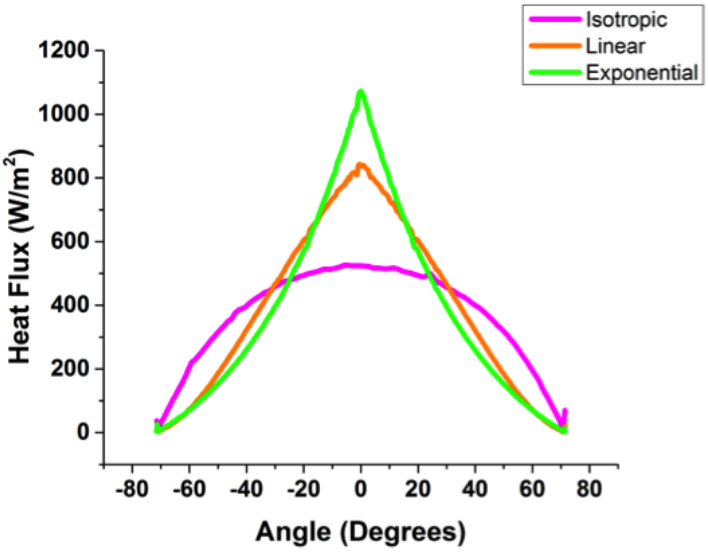

Figure 6.4: Heat flux profiles at edge for lens structure with varying thermal conductivity

6.2 Multi-layered lens based on Effective Medium Approach

Materials with varying thermal conductivity are generally rare in nature, thus we explore ways to make geometries with varying thermal conductivity. One way of engineering such geometries is by making a multi-layered structure, with successive layers being of different thermal conductivity. Using an effective medium like approach, we can make geometries by changing the number of layers / decreasing the layer thickness. Properties of such materials will then asymptotically get

closer to materials with perfectly varying properties, thermal conductivity in our case with decreasing successive layer thickness.

To explore this effect, we take the rectangular geometry we have discussed previously and shown in figure 6.5, and change the lens geometry to a multi-layered one. We take the thermal conductivity of the layers on the edge to be 0.5 W/mK and center most layer to be 4 W/mK similar to what we did earlier. We increase the number of layers from 5 to 51 corresponding to layer thickness of 6 mm to 0.6 mm, and plot the heat flux at the edge of the lens. We see from the plot of heat flux plotted from the edge of the geometry to the center, as the number of layers is increased (figure 6.6), the heat flux profile gets less discrete and seems to be getting closer to the linear profile for a perfectly linearly changing lens. To quantify this effect, we follow the approach of Vemuri and Bandaru [33], and calculate the area under the plot (with units of W/m) for each of the lens geometry, and notice the ratio of area of plot for multi-layered case / area of the perfectly linear conductivity plot approaches 1 as number of layers is increased. We can also convert this area under the plot to power by multiplying by the thickness of the setup, and see similar behavior for power (power for linear conductivity material = 0.02974 W) with increasing number of layers (figure 6.7). Thus we can use a multi-layered engineered meta-material based approach to create geometries with varying thermal conductivity to concentrate heat flux. Subsequently we can also use this multi-layered approach to make geometries with reducing length as shown in figure 6.3, which will be discussed in the next chapter.

Some material from this chapter is currently being prepared for submission for publication. The dissertation author, Rahul S. Kapadia was the primary investigator and author of this material.

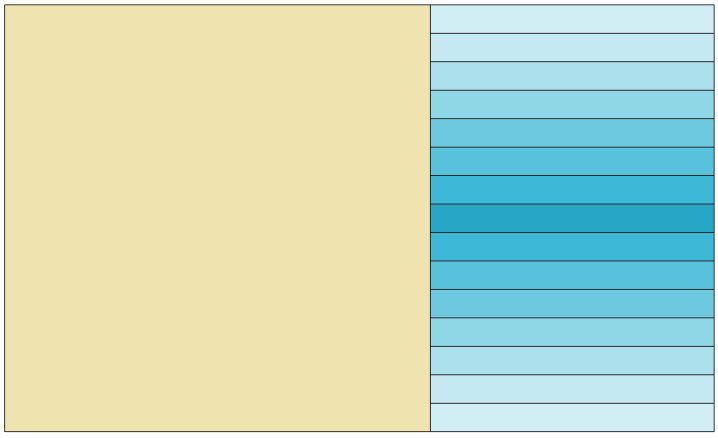

Figure 6.5: Rectangular geometry used to explore the effects of increasing number of layers in the lens

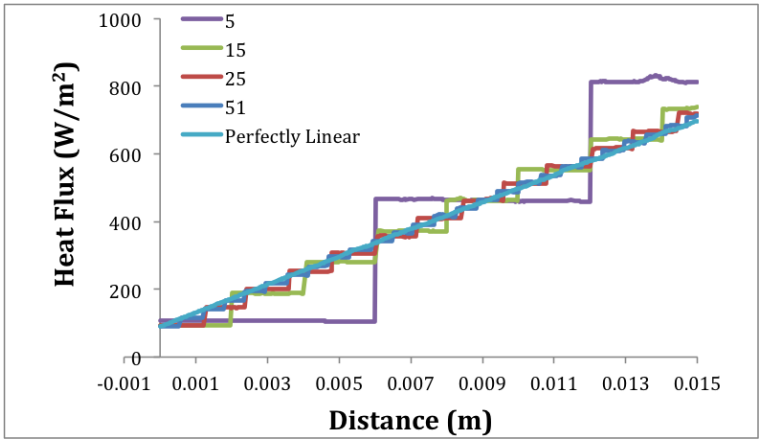

Figure 6.6: Heat flux profile at edge for a straight edged structure shown in figure 2 with increasing number of layers

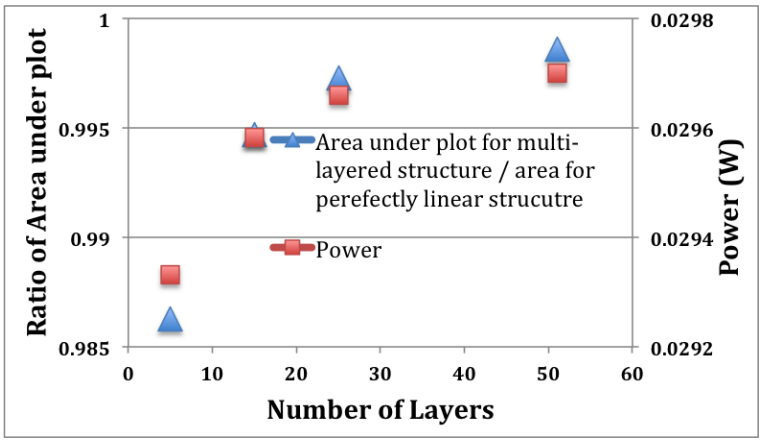

Figure 6.7: Ratio of area under plot for multi-layered structure / perfectly linear conductivity structure and Power plotted with increase in number of layers.

7 Experimental demonstration for heat flux concentration

We have shown in the previous section, that we can device a multi-layered geometry with successive layers of different thermal conductivity to make a device which would mimic a anisotropic material device.

For making a thermal concentration, we use the previously characterized MWCNT - RET polymer composite.

7.1 Experimental design of lens structure

To make this lens structure, we pick nanotube composites with discrete thermal conductivity values. We were able to pick 6 composites which had a definite variation in their measured conductivity values. For ensuring that each layer has a measurable effect in concentration of heat flux, we keep each layer to be $\sim$ 2 mm in thickness. We used a hot press as discussed in chapter 2 to make these layers. For ensuring uniform thickness of each layer, we fabricated Aluminum molds corresponding to the layer dimensions. We also made a special mold with an angle on of the edges to make layers for the reducing geometry setup.

A representative figure with MWCNT concentration for each layer is shown below. We take the edge layers to be with volume fraction of 0.4 % with κ = 0.34 W/mK, while the center most layer has a volume fraction of 10 % with κ = 0.6 W/mK. We use Arctic Silver Thermal adhesive between each layer to ensure minimum thermal resistance between successive layers. To explore how interface thermal resistance would have an effect on the flux concentration, we performed

simulations by taking thermal conductivity of the layer to be from 0.01 W/mK to 1 W/mK, and see that a 100 Micron interface layer does not have any adverse effect on the overall heat flux concentration.

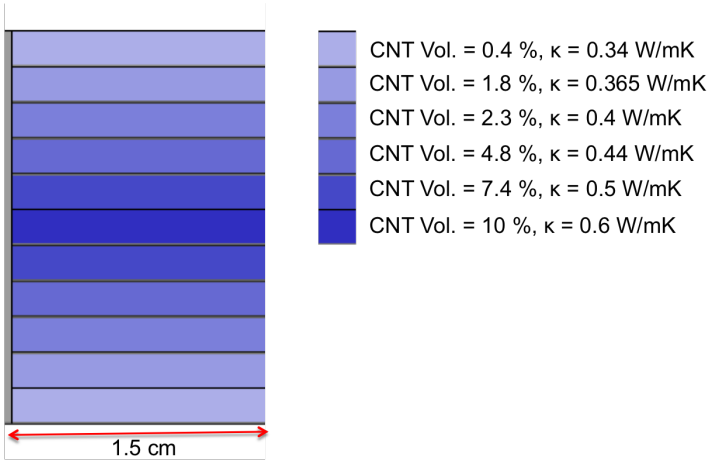

Figure 7.1: Geometry showing multi-layered lens structure with MWCNT volume fraction for each layer

For the source block, we use acrylic block with length of 3 cm. To ensure uniform cold temperature boundary conditions at the edge of lens, we take a copper block.

Experimental geometries were devised for 2 different cases. First case involved a rectangular geometry lens with length of each layer to be 1.5 cm, and width being 1 cm. In this case we expect to see heat flux concentration because of the thermal conductivity contrast of the layers. We take 1 cm long copper block as the sink. Second case involved a reducing geometry lens with reducing length as we go from edge to the center. We keep the length of the layer at the edge to be 1.5 cm, and then keep a 45° angle as the length of layers is reduced going to center. The copper sink block is made with a corresponding shape to fit perfectly with the lens.

We use arctic silver 5 thermal interface material between the acrylic block and lens, and also the lens and the copper block. All the three devices were painted black to ensure uniform high emissivity (ϵ) to ensure accurate temperature measurements using the IR Camera. Lamp black paint has a generally accepted

value for $\epsilon \sim 0.95$. All the other surfaces were painted with the low emissivity paint (LO/MIT-II MAX) and shielded with a radiation shield to ensure minimum radiative and convective heat losses. LO/MIT-II MAX has an $\epsilon \sim 0.15$ when painted using an airbrush over a polymer surface.

The radiation shield is also placed on top of the hot copper block. This ensures a similar temperature gradient being setup in the polymer shield. By placing the radiation shield really close to the experimental setup, and maintaining a similar temperature gradient, we ensure minimum convective losses.

We performed simulations in COMSOL by taking these emissivity values, and a convective heat transfer coefficient of 5 W/m^2K, and observe minimal effect on the concentration effects.

7.2 Rectangular Geometry Lens

To explore the effect heat flux concentration, by thermal conductivity, we performed multiple experiments with the rectangular geometry lens. From the COMSOL simulation, we see how the flux profile would be discrete and be directly proportional to the layer's thermal conductivity. For T_{hot} = 380 K, and T_{cold} = 278, we can see the heat flux at the edge of the lens structure as seen in the figure below. The heat flux concentration ratio which we take as ratio of heat flux at the center layer to the heat flux at the edge most layer is equal to ~ 1.68, which is the ratio of the thermal conductivities of the center layer to the edge most layer.

We see from experimental measurements using IR camera, that the temperature contours obtained look quite similar to what is predicted by COMSOL simulations. For these specific temperature condition, the heat flux profile can then be extracted from Comsol and is depicted in the figure below. To check the simulation's closeness to the experiments, we calculated the heat flux in the source block and we estimate a value of $\sim$ 466 W/m^2 (estimated through the ratio of the temperature drop across the acrylic of $\sim$ 70 K to the thermal resistance: $L_{acrylic}$ (=3 cm) / $\kappa_{acrylic}$ (=0.2 W/mK), which compares to the what is observed in the simulation of $\sim$ 505 W/m^2. We have also made rough estimate of the heat flux

at the edge of the lens / sink interface in the experiment by taking a simple 1-dimensional Fourier law, normal to the temperature iso-contours, and see values within 10 % of the simulations.

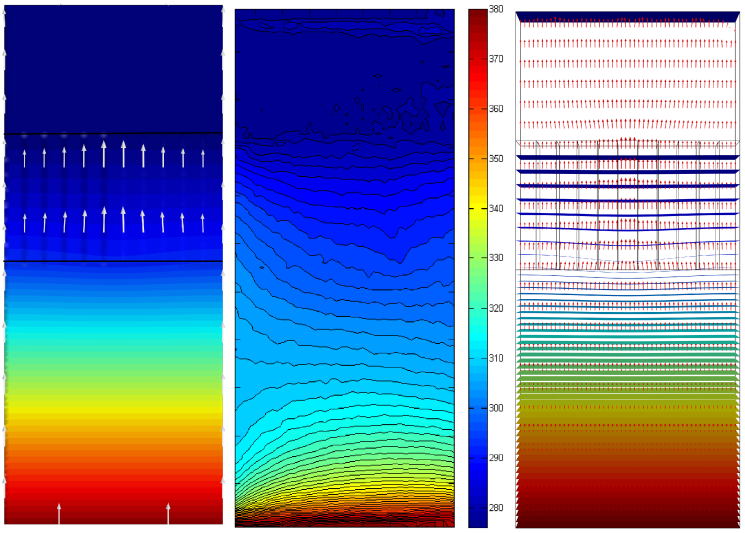

Figure 7.2: Figure on Left shows temperature contours obtained from COMSOL, center figure show the experimental temperature contours, while the figure on right denotes the corresponding heat flux vectors

To see how the heat flux profile across the cross-section of the geometry from the source to the sink, we plot it at four different cross-sections and see the profiles in the source block, at the source - lens interface, lens - sink interface and finally in the sink. To make sure our simulations were accurate, we calculated the area under the plot for each cross-section, and confirm that they are equal ensuring a conservation of energy.

7.3 Reducing Geometry Lens

In this case we explore the effect of heat flux concentration, by a combination of thermal conductivity and length, we performed multiple experiments with the rectangular geometry lens. From the comsol simulation, we see how the flux will be concentrated due to this coupled effect. For T_{hot} = 378 K, and T_{cold} = 280 K, we can see the heat flux at the edge of the lens structure as seen in the figure

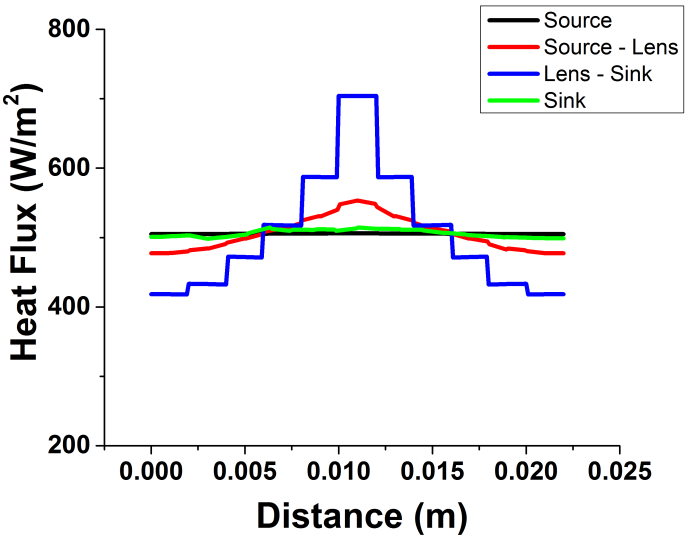

Figure 7.3: Heat flux at multiple cross-sections of the setup for a Rectangular lens

below. The heat flux concentration ratio which we take as ratio of heat flux at the center layer to the heat flux at the edge most layer is equal to ~ 8, we take heat flux over the entire layer thickness of 2 mm, to negate the boundary layer effects. We calculated the heat flux in the source block and we estimate a value of ~ 500 W/m^2 (estimated through the ratio of the temperature drop across the acrylic of ~ 75 K to the thermal resistance: $L_{acrylic}$ (=3 cm) / $\kappa_{acrylic}$ (=0.2 W/mK), which compares to the what is observed in the simulation of ~ 502 W/m^2.

We seem from experimental measurements using IR camera, that the temperature contours obtained look quite similar to what is predicted by COMSOL simulations. For these specific temperature condition, the heat flux profile can then be extracted from COMSOL as before and is depicted in the figure.

We explore how the heat flux profile across the cross-section of the geometry from the source to the sink similar to what we do for the rectangular geometry, we plot it at four different cross-sections and see the profiles in the source block, at the source - lens interface, lens - sink vertical interface and finally in the sink. To make sure our simulations were accurate, we calculated the area under the plot for each cross-section, and confirm that they are equal.

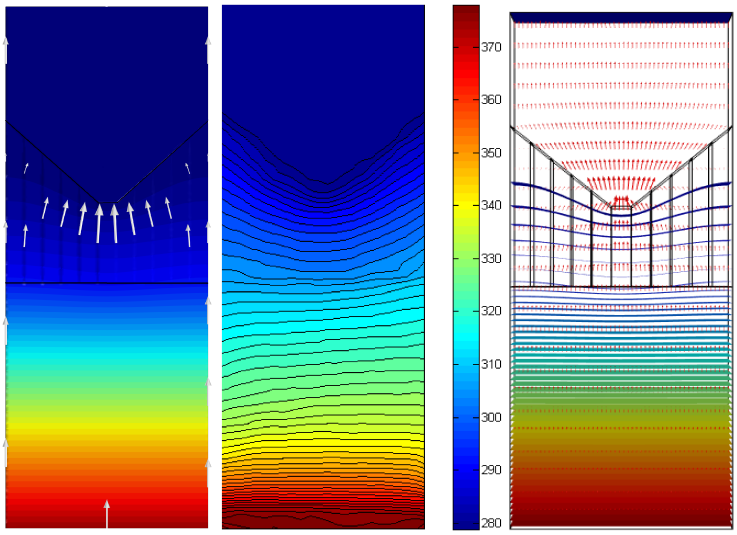

Figure 7.4: Figure on Left shows temperature contours obtained from COMSOL, center figure show the experimental temperature contours, while the figure on right denotes the corresponding heat flux vectors

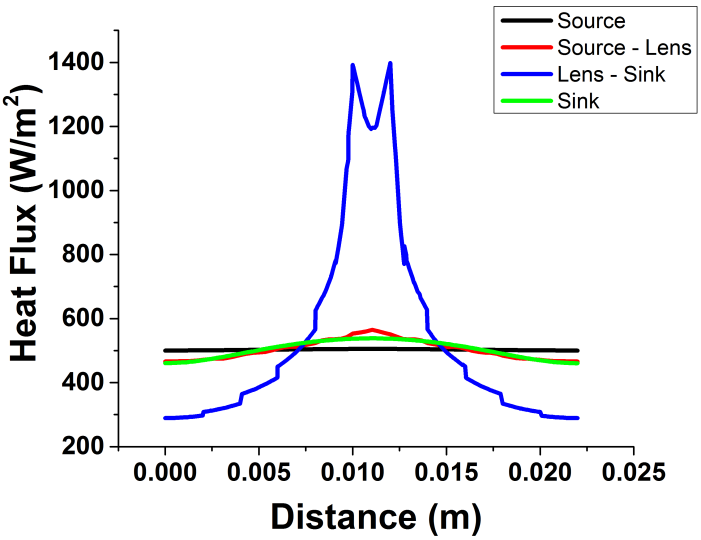

Figure 7.5: Heat flux at multiple cross-sections of the setup for a Reducing lens

Comparing this concentration to what is predicted for the rectangular geometry case, we see how the coupling of thermal conductivity and length results in a much higher concentration of heat flux. We see the heat flux at the center is more than ~ 3 times higher in the reducing case.

7.4 Heat Flux Concentration Effect Measurements

All our previous experimental measurements proved heat flux concentration by using a multilayered variable thermal conductivity polymer. Subsequently we wanted to demonstrate a practical effect of the heat flux concentration. We considered various options to harness this concentration. We considered using Thermoelectric generators (TEG) to get this effect. Thermoelectric generators generate a voltage when they a subjected to a temperature gradient. Heat flux passing through the generators, would generate a temperature gradient which would manifest into a generated voltage, which could be subsequently measured. We also explored fabricating and using a setup which would heat a liquid using the concentrated heat flux. After running some simulations, we decided to not pursue liquid heating, as it would have resulted in really complicated experiments.

For using TEG, we explored setups where we put multiple TEG's across the cross-section of the setup being tested. If we show one TEG generating higher voltage than another one, that would imply that TEG being subjected to higher heat flux. The voltage being generated can be measured by a Keithley 2700 Digital Multimeter.

7.4.1 TEG Calibration

We ordered various TEG's from Digikey with different dimensions.To calibrate the TEG before using them, we mounted the them on a copper plate mounted on top of a Peltier Cooler. Using two surface mount k-type thermocouples, we measured the temperature on the top and the bottom surface of the Peltier cooler. By increasing the power to the Peltier cooler, we were able to measure voltage generated by a DMM. Plotting the DMM voltage against the temperature difference

between the top and the bottom surfaces, we were able to get the sensitivity of the TEG. We got a good linear fit for our measured data, and the sensitivity was extracted to be 14.5 $\sim$ mV / K for the bigger TEGs and to be $\sim$ 2.5 mV / K. Setup for calibration can be seen in figure 7.2, while the sensitivity curves for two TEG's we used can be seen in figures 7.3 & 7.4.

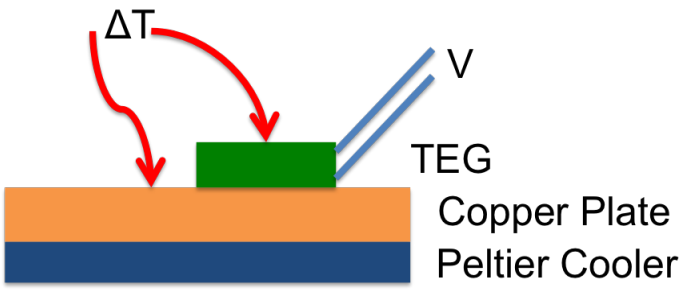

Figure 7.6: Setup for calibration for TEG

Figure 7.7: One of the TEGs used in our experiments

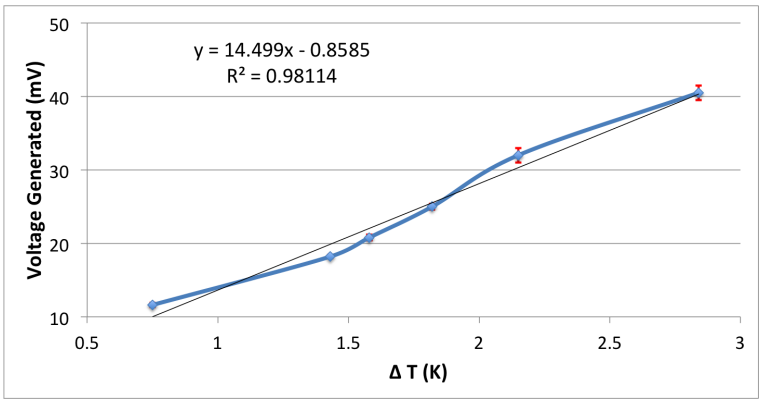

Figure 7.8: Calibration plot for big TEG, we observe a sensitivity of $\sim$ 14.5 mV/K

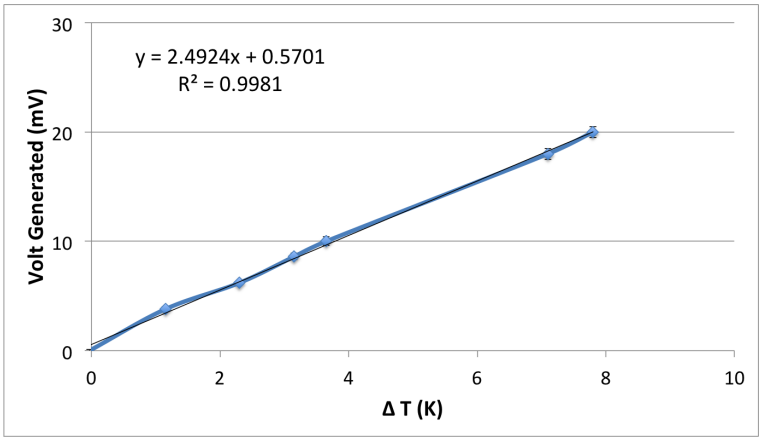

Figure 7.9: Calibration plot for small TEG, we observe a sensitivity of $\sim$ 2.5 mV/K

7.4.2 Concentration experiments with TEG

For the rectangular lens, we used three TEGs as shown in figure 7.10. As predicted by our earlier simulations and experiments we expect the center TEG to generate a higher voltage. Using the sensitivity, we can convert the generated voltage into a ΔT across the TEG length. As the cold sider temperature is kept constant for all the TEGs by using the Copper block mounted to the cold plate, we expect the hot side temperature to be a direct function of the subjected heat flux. We performed simulations and observed average hot side temperature for center TEG to be 1.43 times the average hot side temperature for the side TEGs.

Experimental temperature contours can be seen from figure 7.11, and they compare quite well with the ones predicted by simulations. Plotting the ΔT against the position of the TEG, we notice for various Acrylic block Hot temperature conditions (T_{hot} = 329 K - 400 K), the ΔT at center is higher than the ones at side. Also ΔT_{side} for both sides is also quite similar. Taking the average ratio of ΔT_{center} to ΔT_{side}, we get a value of 1.40, which compares quite well with the 1.32 value predicted by simulations.

For the reducing lens, we used four TEGs as shown in figure 7.12. We performed experiments using two different size TEGs. For the smaller TEGs we were only able to get data for one of the sides, as the other TEG had a malfunction at the time of the experiment. We were able to get all four sets of measurements for the bigger size TEGs. We see for the both the cases, ΔT_{center} is much higher than ΔT_{side}, proving heat flux concentration. For the average ratio of ΔT_{center} to ΔT_{side}, we get a value of 1.50 for the bigger TEGs and yy for the smaller TEGs.

From all our experiments for both the rectangular and the reducing geometry lens, we show measurable effect of heat flux concentration, and thus prove how these concentrators could be used for practical concentration of heat flux.

Some material from this chapter is currently being prepared for submission for publication. The dissertation author, Rahul S. Kapadia was the primary investigator and author of this material.

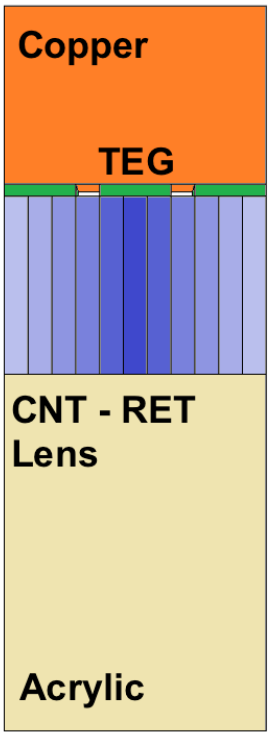

Figure 7.10: Schematic for experimental setup showing position of TEG for Rectangular geometry lens

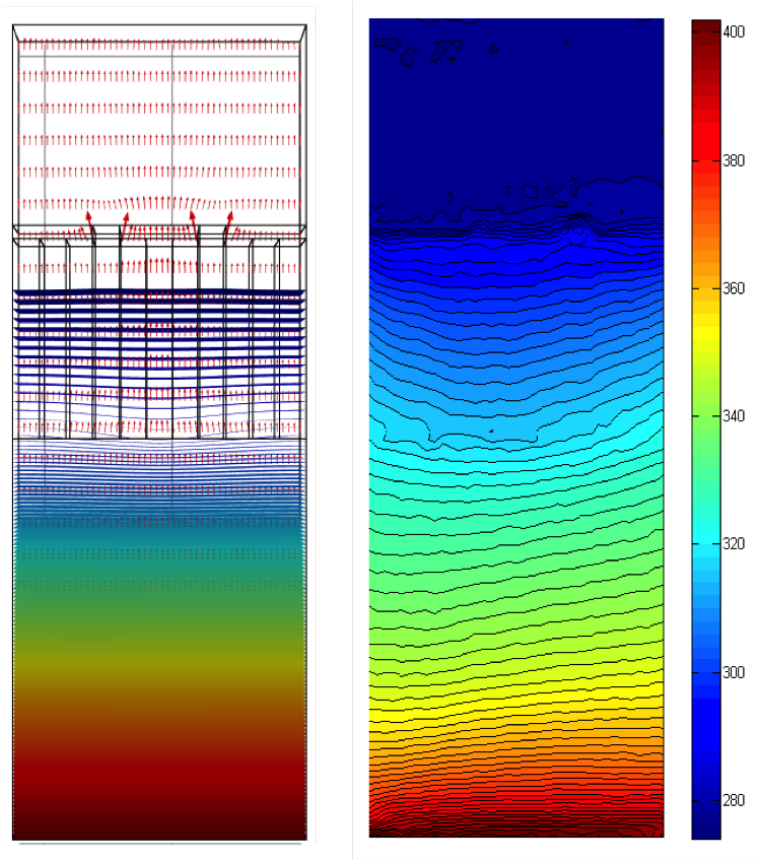

Figure 7.11: Figure on left shows the temperature iso-contours and heat flux in COMSOL simulation, while on the right is the experimental iso-contours obtained by IR Camera for rectangular geometry lens

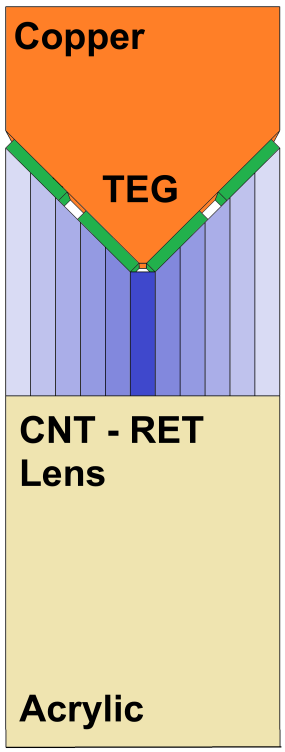

Figure 7.12: Schematic for experimental setup showing position of TEG for Reducing geometry lens

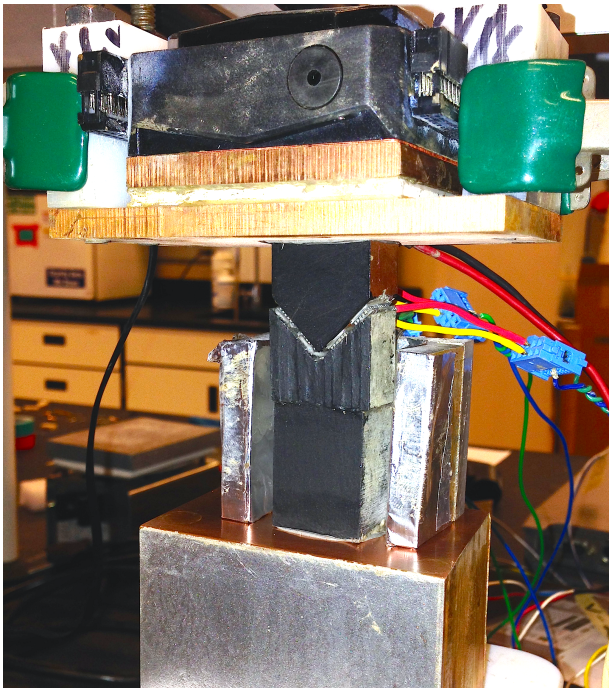

Figure 7.13: Actual experimental setup showing position of TEG for Reducing geometry lens

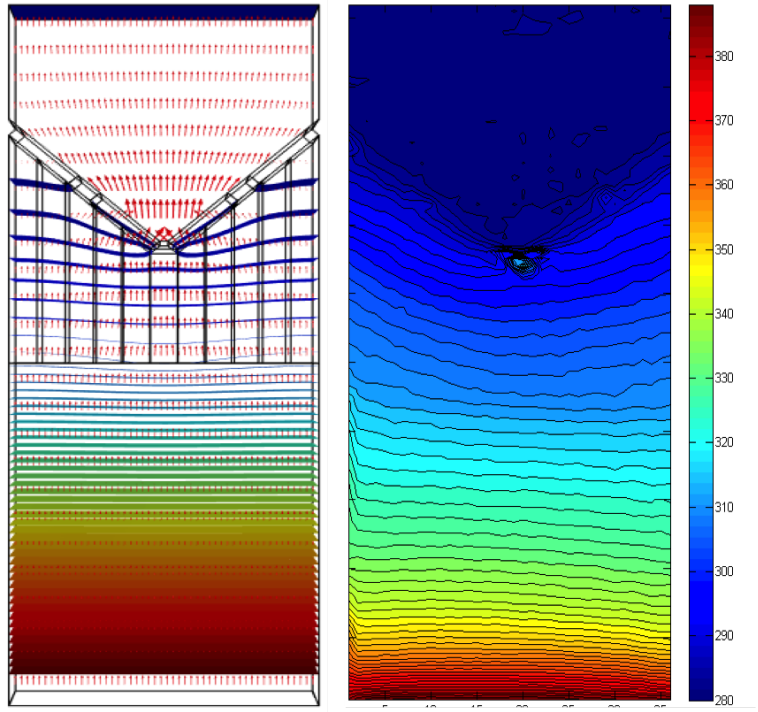

Figure 7.14: Figure on left shows the temperature iso-contours and heat flux in COMSOL simulation, while on the right is the experimental iso-contours obtained by IR Camera for reducing geometry lens

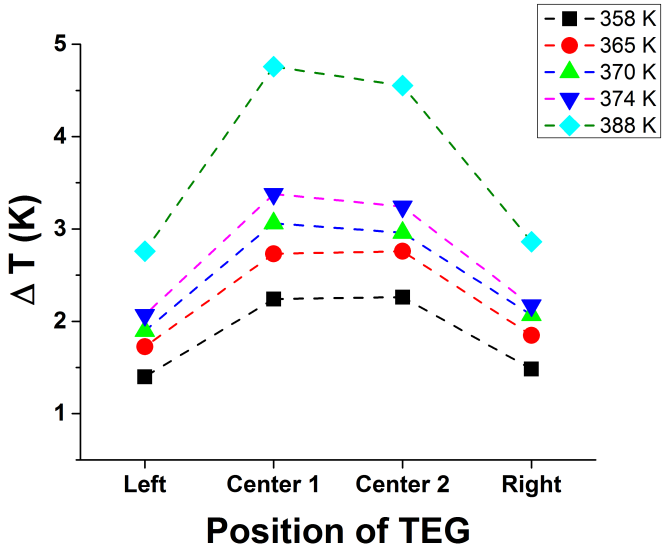

Figure 7.15: ΔT vs position of Big TEG for Reducing geometry lens

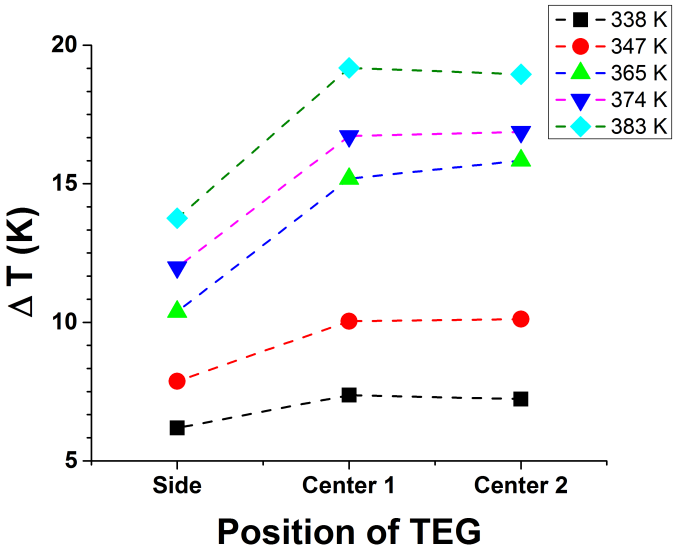

Figure 7.16: ΔT vs position of Small TEG for Reducing geometry lens

8 Experimental demonstration for heat flux homogenizer

A thermal concentrator device was explored and demonstrated in the previous chapter. In this chapter, we will discuss another type of thermal device in form of a thermal homogenizer.

It was shown previously, how geometrical effects result in concentration of heat flux. If heat flux was being transported from a higher cross-sectional area to a lower cross-sectional area, there would be flux concentration at the center as the thermal resistance would be lower at the center.

We show a specific case of this geometrical concentration in figure 8.1. A device with changing cross-sectional area links the two devices, which we will call as source and sink. If we plot heat flux along the cross-section in the varying cross-section device, we see how the heat flux profile shows clearly the concentration.

To prevent this concentration, we device a multi-layered thermal homogenizer. We know as previously discussed heat flux follows the path of least thermal resistance ($R_{th} = L/\kappa$). Thus if we wanted to prevent heat flux to get concentrated at the center of the device, we would need to ensure thermal resistance is maintained constant along the homogenizer device which would prevent concentration of heat flux.

8.1 Analytical design of Thermal Homogenizer

To make a homogenizer device, we use the multi-layered approach we used earlier. In this case we take the source block to have a 5 x 5 x 5 cm block with κ

= 1 W/mK, and the sink block to of copper and have a 0.5 x 0.5 cm cross-section, and 1 cm in length.

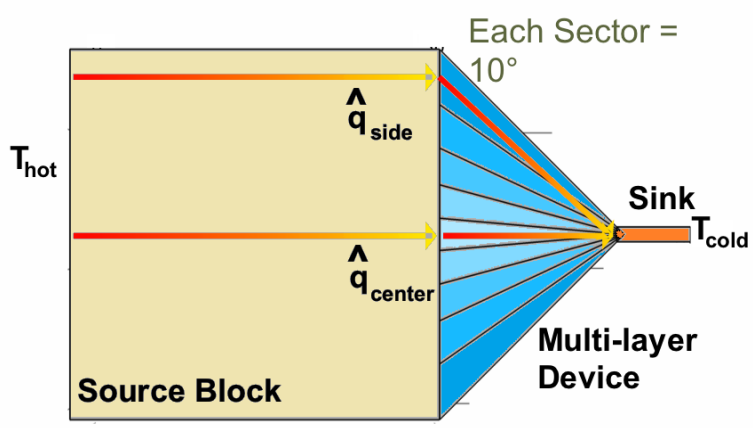

Figure 8.1: Geometry for analytical formulation of a thermal homogenizer

We show thermal resistance for 2 representative heat flux vectors going from the source to the sink. For the heat flux vector at the center, the thermal resistance is given by $R_{th-center}$, while thermal resistance at any other location is given by $R_{th-side}$. To maintain a uniform / homogeneous flux in the device, we will need to ensure $R_{th-center} = R_{th-side}$. We divide the device into 9 layers with each layer with a sector angle of 10 °. This can be further given as

$$\frac{L_{center}}{\kappa_{center}} = \frac{L_{side}}{\kappa_{side}} \tag{8.1}$$

From geometry, we can find relation between the length parameter for successive layers as

$$L_{side} = \frac{L_{center}}{cos\theta_{side}} \tag{8.2}$$

Here θ is the angle between the center of the geometry and the center of the respective layer in consideration.

Thus we get the following relation between κ of successive layers

$$\kappa_{side} = \frac{\kappa_{center}}{cos\theta_{side}} \tag{8.3}$$

By picking successive layers with the relation we derived earlier, we can thus ensure each layer to have similar thermal resistance and thus ensuring uniform heat flux across the cross-section. For our simulations, we take $\kappa_{center} = 2$ W/mK. We compare this multi-layer, constant thermal resistance geometry with an isotropic material device (with average value for thermal conductivity ~ 2.2 W/mK) for $T_{hot} = 350$ K and $T_{cold} = 280$ K, and see heat flux across the device cross-section is much more homogenous in the constant resistance case as seen in figure 8.2 & 8.3.

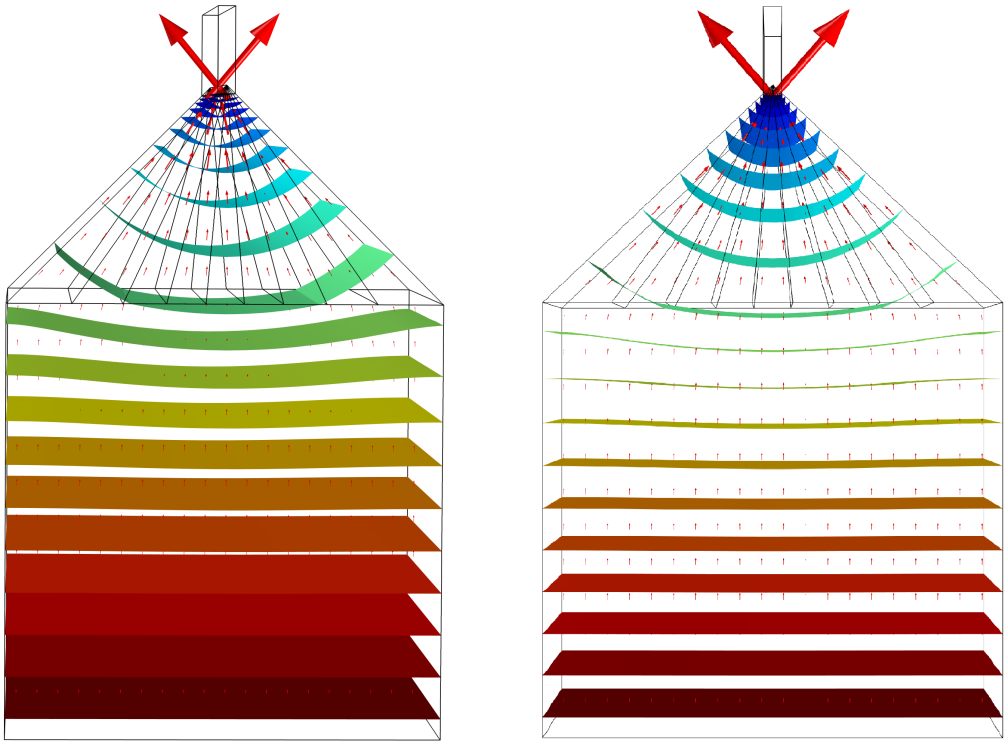

Figure 8.2: Figure on left shows temperature contours and heat flux for an isotropic conductivity material device, while figure on right shows temperature contours and heat flux for a constant thermal resistance device

8.2 Experimental design of Thermal Homogenizer

For making an experimental homogenizer device, we take an Acrylic block as the source block. For making the multi-layered device, we take the center layer

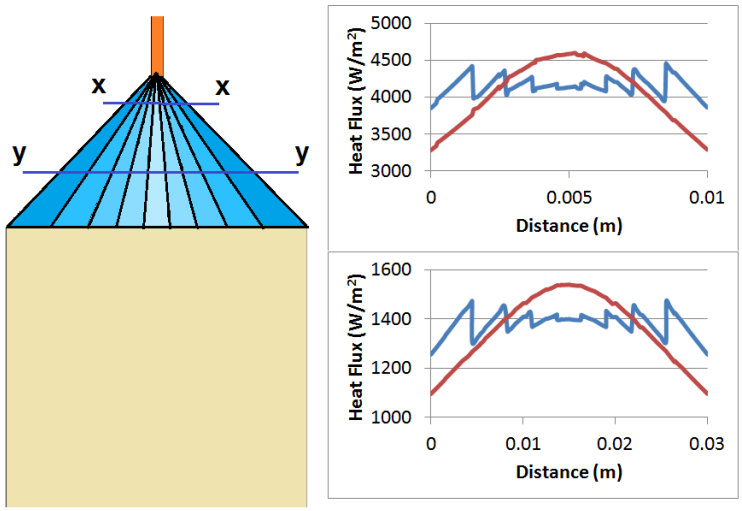

Figure 8.3: Heat flux comparisons at two different cross-sections for the device. Figure on top shows flux at x-x cross-section, while figure at bottom shows flux at y-y cross-section

to be made from 0.4 % CNT RET polymer with $\kappa = 0.34$ W/mK. Using the geometrical relation we derived earlier, we pick 4 other polymer composites with suitable thermal conductivity. We take a copper block to be the sink. The acrylic source has a width of 6 cm, while the copper block has a width of 2 cm. All the dimensions of the complete experimental setup can be seen in figure 8.4, with thickness of the complete setup being 6 mm. We use Arctic Silver Thermal adhesive between each layer to ensure minimum thermal resistance between successive layers.

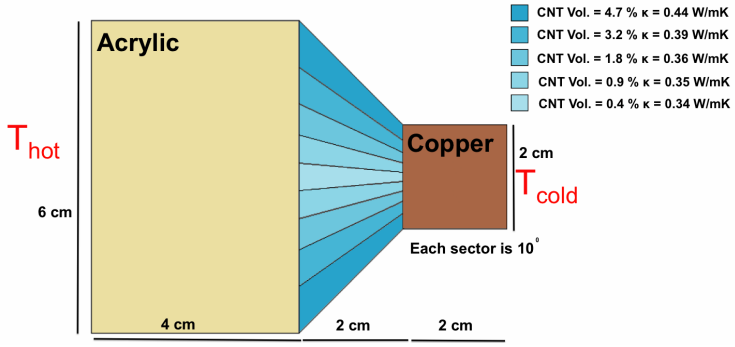

Figure 8.4: Geometry for experimental demonstration of a thermal homogenizer

Using the IR camera setup, we perform experiments with $T_{hot} = 374$ K, and

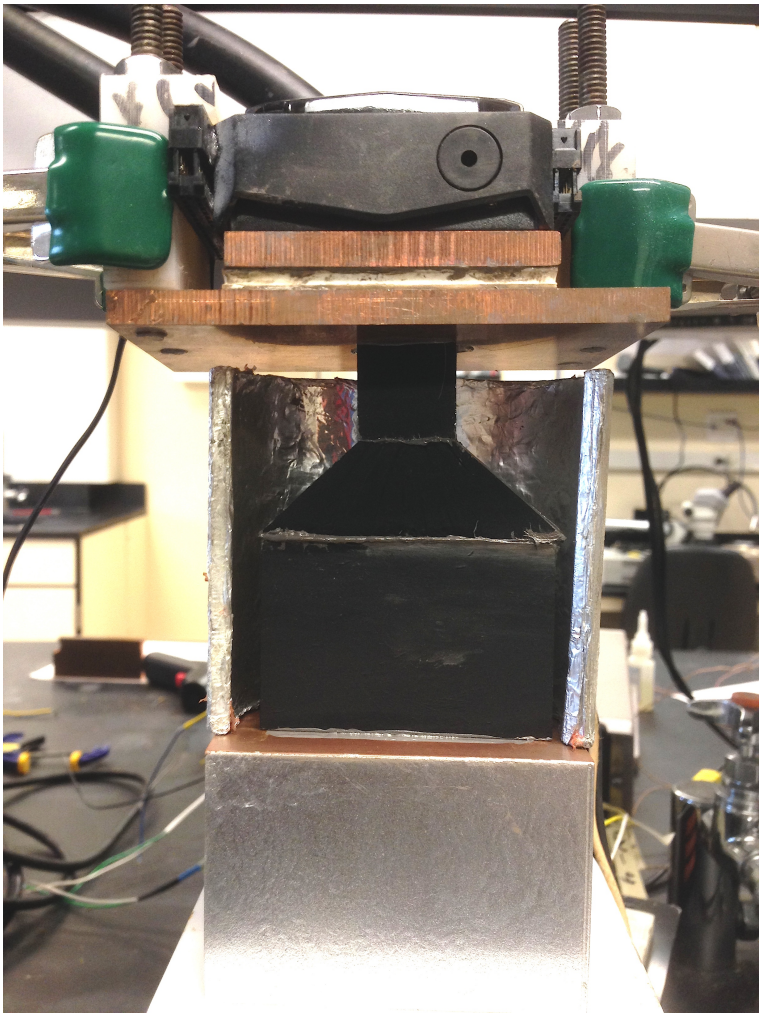

Figure 8.5: Experimental setup of a thermal homogenizer

T_{cold} = 285 K. We can see from figure yy, how the temperature contours obtained with the IR camera compare quite well with the ones we observe in the COMSOL simulation. For these specific temperature conditions, the heat flux profile can then be extracted from our simulations and is depicted in the figure 8.6.

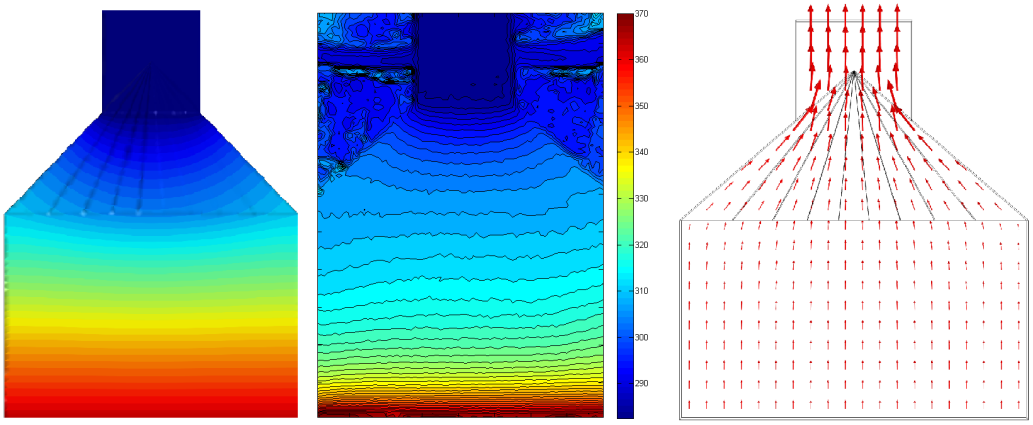

Figure 8.6: Figure on left shows the temperature contours obtained from COMSOL, while the center figure shows experimental temperature contours, the figure on the right shows the corresponding heat flux vectors

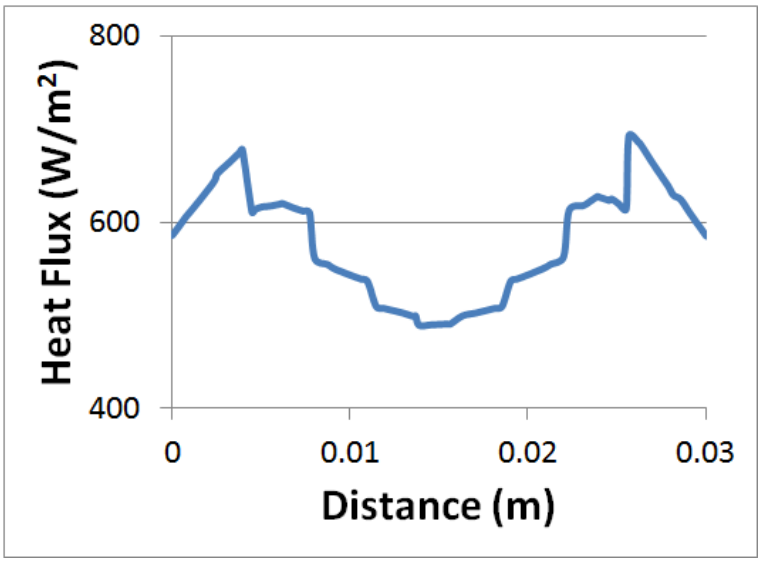

Figure 8.7: Uniform heat flux observed across the cross-section of the homogenizer

As seen in figure 8.7, we see from the simulations, the homogeneity of heat

flux across the device cross-section, proving the validity of our methodology to get uniform heat flux.

Some material from this chapter is currently being prepared for submission for publication. The dissertation author, Rahul S. Kapadia was the primary investigator and author of this material.

9 Conclusions

9.1 Summary

In my study to control conductive heat flux, I have shown both analytically and through experiments ways to control and direct conductive heat flux. Most of my formulations were done by formulations of minimization of the thermal resistance and also by suitable use of the Fourier law of heat conduction at a macro scale.

I have also analyzed and characterized the thermal conductivity enhancements of a multi-walled carbon nanotube polymer composite with increasing filler content. I have shown by experimental measurements and subsequent analytical work, how percolation effects are precluded in these enhancements and an Effective medium type approach can be used to fit these increases with increasing filler content. The values of thermal conductivity increased from 0.32 W/mK to 0.6 W/mK for a 10 % volumetric nanotube filler content in the composite.

Using the Fourier law based heat conduction manipulations, I have devices two thermal devices - Thermal flux concentrator and Thermal homogenizer. Using a rectangular thermal concentrator, I was able to obtain a flux concentration of $\sim$ 1.5 times at the center compared to the edge. For a reducing geometry setup, much higher flux concentrations were observed. I was also able to show experimental flux concentration using Thermoelectric generators by converting the applied heat flux to a measurable temperature difference across the generator. For this, I measured a $\sim$ 1.43 times higher flux at center for a rectangular geometry, while a $\sim$ 1.52 times higher flux was noted at center for a reducing compared to the values at side.

9.2 Future Work

All my work has opened up endless possibilities for further work. My flux control simulations and experiments have demonstrated a simple method to control heat flux using the Fourier law. Much further analytical work can be done in analyzing how the combination of length and thermal conductivity is coupled together to get heat flux variations. I strongly believe an equation can be derived similar to the lens-maker equation which is used for design of optical lens, to design thermal lenses. Such study would also generate further insights for developing other thermal devices.

My study has indicated the seminal development of thermal lenses, leading to the concentration of heat flux, using polymeric materials. While the research constitutes an excellent proof of principle, further issues related to thermal mode characterization, interfacial thermal resistance (R_{int}), etc. need to be better understood. Such aspects would lead to the fruitful utilization of the thermal resistance minimization principle and the resultant development of new technologies aimed at improving energy efficiency through control and manipulation of waste heat.

This study can quite easily be adopted for making practical devices and for addressing real world thermal challenges. Using a multi-layered approach could prove difficult in making real world devices, but with the advent of additive manufacturing, I am sure we will be able to make geometries with inbuilt anisotropy for thermal conductivity by changing the filler content in successive layers being deposited. This could result in lot of interesting applications for thermal flux control, and can even be used to make thermal guides / channels to protect delicate electronic equipment.

Next step in terms of experiments, would be formation of a bigger lens geometry and then use sunlight and concentrate the heat on a thermoelectric generator. If an experiment can be devised to show higher power generation using a thermal concentrator, it could result in lot of practical applications for this technology.

One such example for utility can be seen in figure 9.1. Sun's spectrum contains of wavelengths of quite a wide range of wavelengths. Photovoltaic cells

can generally only utilize a narrow range of the available wavelengths. If a wavelength segregator is used to separate the lower wavelength radiation from the higher wavelength one, the lower wavelength radiation can then be made incident on the photovoltaic module which can convert that to electricity. The higher wavelength radiation which is in the infra-red range contains most of the incident heat. This radiation spectrum can then be absorbed by a black body absorber and then concentrated on a thermoelectric generator by using a heat concentration lens. Thus by using a combinator of photovoltaic cells and thermoelectric generator using a concentration lens, we can utilize majority of the spectrum of the sun.

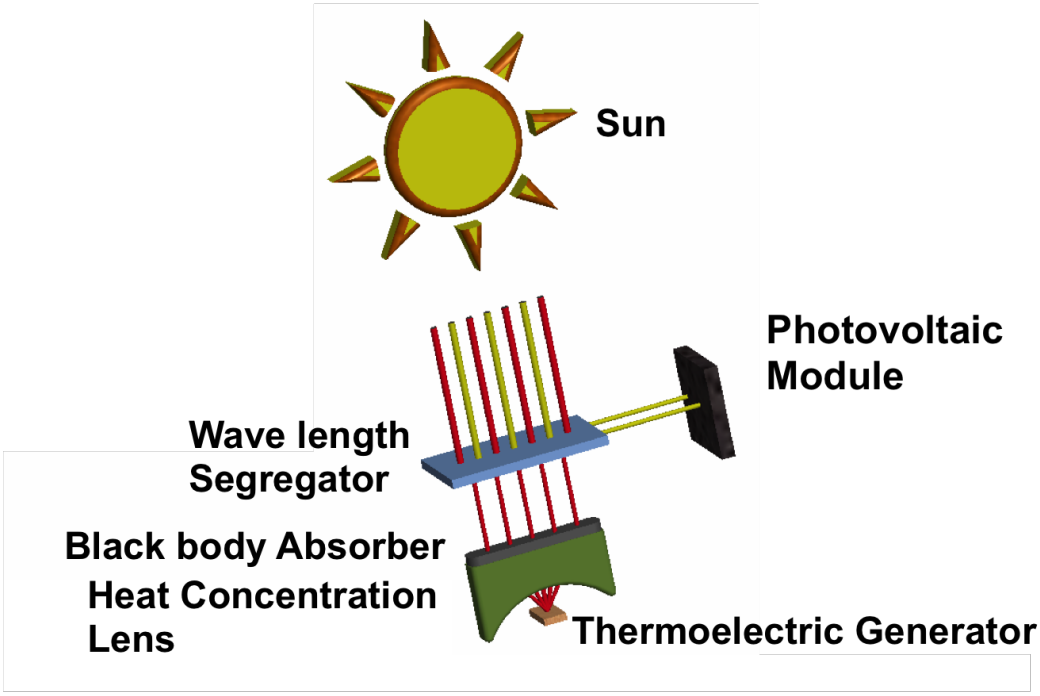

Figure 9.1: Utilization of sun's spectrum to generate electricity by a combinator of photovoltaic cells and thermoelectric generator.

Bibliography

[1] A. Tan and L. R. Holland. Tangent law of refraction for heat conduction through an interface and underlying variational principle. *American Journal of Physics*, 58(10):988–991, 1990.

[2] Anthony F Mills. *Heat Transfer*. Prentice Hall, 1998.

[3] Chauncey Starr. The copper oxide rectifier. *Journal of Applied Physics*, 7(1):15–19, 1936.

[4] Nianbei Li, Jie Ren, Lei Wang, Gang Zhang, Peter Hänggi, and Baowen Li. *Colloquium* : Phononics: Manipulating heat flow with electronic analogs and beyond. *Rev. Mod. Phys.*, 84:1045–1066, Jul 2012.

[5] ES Dettmer, BM Romenesko, HK Charles, BG Carkhuff, and DJ Merrill. Steady-state thermal conductivity measurements of a1n and sic substrate materials. *IEEE Transactions on Components Hybrids and Manufacturing Technology*, 12(4):543–547, DEC 1989.

[6] David G. Cahill. Thermal conductivity measurement from 30 to 750 k: the 3 omega method. *Review of Scientific Instruments*, 61(2):802–808, 1990.

[7] ASTM Standard E1225. Standard test method for thermal conductivity of solids by means of the guarded-comparative-longitudinal heat flow technique. *ASTM International, West Conshohocken, PA, 2003, DOI: 10.1520/E1225-09, www.astm.org*, 2009.

[8] ASTM Standard D5470. Standard test method for thermal transmission properties of thermally conductive electrical insulation materials. *ASTM International, West Conshohocken, PA, 2003, DOI:10.1520/D5470-12, www.astm.org.*, 2012.

[9] M. M. Yovanovich and E. E. Marotta. *Heat Transfer Handbook, A. Bejan and A. D. Kraus, Editors*. Wiley, 2003.

[10] Akhan Tleoubaev, Andrzej Brzezinski, and Luiz Claudio Braga. Accurate simultaneous measurements of thermal conductivity and specific heat of rub-

ber, elastomers, and other materials. In *Proceedings of 12th Brazilian Rubber Technology Congress*, 2008.

[11] Duncan M. Price and Mark Jarratt. Thermal conductivity of ptfe and ptfe composites. In *Proceedings of The Twenty-Eight Conference of The North American Thermal Analysis Society, Orlando, Florida*, 2000.

[12] Sung-Hoon Park, Paul T. Theilmann, Peter M. Asbeck, and Prabhakar R. Bandaru. Enhanced electromagnetic interference shielding through the use of functionalized carbon-nanotube-reactive polymer composites. *IEEE Transactions on Nanotechnology*, 9(4):464–469, JUL 2010.

[13] Sung-Hoon Park and Prabhakar R. Bandaru. Improved mechanical properties of carbon nanotube/polymer composites through the use of carboxyl-epoxide functional group linkages. *Polymer*, 51(22):5071–5077, 2010.

[14] Rahul S. Kapadia, Brian M. Louie, and Prabhakar R. Bandaru. The influence of carbon nanotube aspect ratio on thermal conductivity enhancement in nanotube-polymer composites. *Journal of Heat Transfer*, 136(1):011303, October 2013.

[15] Florian H. Gojny, Malte H.G. Wichmann, Bodo Fiedler, Ian A. Kinloch, Wolfgang Bauhofer, Alan H. Windle, and Karl Schulte. Evaluation and identification of electrical and thermal conduction mechanisms in carbon nanotube/epoxy composites. *Polymer*, 47(6):2036 – 2045, 2006.

[16] MJ Biercuk, MC Llaguno, M Radosavljevic, JK Hyun, AT Johnson, and JE Fischer. Carbon nanotube composites for thermal management. *Applied Physics Letters*, 80(15):2767–2769, APR 15 2002.

[17] D. A. G. Bruggeman. Berechnung verschiedener physikalischer konstanten von heterogenen substanzen. *Ann. Phys. (Leipz.)*, 24:636, 1935.

[18] S. Pfeifer, S.-H. Park, and P. R. Bandaru. Analysis of electrical percolation thresholds in carbon nanotube networks using the weibull probability distribution. *Journal Of Applied Physics*, 108(2):024305, JUL 15 2010.

[19] I. Balberg. Universal percolation-threshold limits in the continuum. *Physical Review B*, 31:4053–4055, 1985.

[20] P. Bonnet, D. Sireude, B. Garnier, and O. Chauvet. Thermal properties and percolation in carbon nanotube-polymer composites. *Applied Physics Letters*, 91(20):201910, NOV 12 2007.

[21] N Shenogina, S Shenogin, L Xue, and P Keblinski. On the lack of thermal percolation in carbon nanotube composites. *Applied Physics Letters*, 87(13):133106, SEP 26 2005.

[22] Rolf Landauer. Electrical conductivity in inhomogeneous media. *AIP Conference Proceedings*, 40(1):2–45, 1978.

[23] CW Nan. Physics of inhomogeneous inorganic materials. *Progress in Materials Science*, 37(1):1 – 116, 1993.

[24] CW Nan. Effective -medium theory of piezoelectric composites. *Journal Of Applied Physics*, 76(2):1155–1163, JUL 15 1994.

[25] CW Nan, R Birringer, DR Clarke, and H Gleiter. Effective thermal conductivity of particulate composites with interfacial thermal resistance. *Journal Of Applied Physics*, 81(10):6692–6699, MAY 15 1997.

[26] E. T. Swartz and R. O. Pohl. Thermal boundary resistance. *Reviews of Modern Physics*, 61(3):605–668, Jul 1989.

[27] ST Huxtable, DG Cahill, S Shenogin, LP Xue, R Ozisik, P Barone, M Usrey, MS Strano, G Siddons, M Shim, and P Keblinski. Interfacial heat flow in carbon nanotube suspensions. *Nature Materials*, 2(11):731–734, NOV 2003.

[28] CW Nan, G Liu, YH Lin, and M Li. Interface effect on thermal conductivity of carbon nanotube composites. *Applied Physics Letters*, 85(16):3549–3551, OCT 18 2004.

[29] M. B. Bryning, D. E. Milkie, M. F. Islam, J. M. Kikkawa, and A. G. Yodh. Thermal conductivity and interfacial resistance in single-wall carbon nanotube epoxy composites. *Applied Physics Letters*, 87(16):161909, 2005.

[30] Hongliang Zhong and Jennifer R. Lukes. Interfacial thermal resistance between carbon nanotubes: Molecular dynamics simulations and analytical thermal modeling. *Physics Review B*, 74(12):125403, Sep 2006.

[31] CW Nan, XP Li, and R Birringer. Inverse problem for composites with imperfect interface: Determination of interfacial thermal resistance, thermal conductivity of constituents, and microstructural parameters. *Journal of The American Ceramic Society*, 83(4):848–854, APR 2000.

[32] Supradeep Narayana and Yuki Sato. Heat flux manipulation with engineered thermal materials. *Physical Review Letters*, 108:214303, May 2012.

[33] Krishna P. Vemuri and Prabhakar R. Bandaru. Geometrical considerations in the control and manipulation of conductive heat flux in multilayered thermal metamaterials. *Applied Physics Letters*, 103(13):–, 2013.